energies

MDPI

Article

Regressive and Spatio-Temporal Accessibility of Variability in Solar Energy on a Short Scale Measurement in the Southern and Mid Region of Mozambique

Fernando Venâncio Mucomole [1,2,3,*], Carlos Augusto Santos Silva [4] and Lourenço Lázaro Magaia [5]

[1] CS-OGET—Center of Excellence of Studies in Oil and Gas Engineering and Technology, Faculty of Engineering, Eduardo Mondlane University, Mozambique Avenue Km 1.5, Maputo 257, Mozambique
[2] CPE—Centre of Research in Energies, Faculty of Sciences, Eduardo Mondlane University, Main Campus No. 3453, Maputo 257, Mozambique
[3] Department of Physics, Faculty of Sciences, Eduardo Mondlane University, Main Campus No. 3453, Maputo 257, Mozambique
[4] Department of Mechanical Engineering, Instituto Superior Técnico, University of Lisbon, 1600-214 Lisbon, Portugal; carlos.santos.silva@tecnico.ulisboa.pt
[5] Department of Mathematics and Informatics, Faculty of Science, Eduardo Mondlane University, Main Campus No. 3453, Maputo 257, Mozambique; lourenco.l.magaia@uem.mz
* Correspondence: fernando.mucomole@uem.mz or fernandomucomole1@gmail.com

Abstract: Solar energy reaching a horizontal surface can possess fluctuations that impact electricity generation at a solar plant. Despite this, energy access remains inadequate, particularly in rural areas, with an estimated 82% deficiency. This drives us to assess the regressive and spatial-temporal accessibility of solar energy in the southern and mid regions of Mozambique. This evaluation aims to determine the actual availability of energy for electrification purposes. Data on global horizontal irradiation from approximately 8 stations across all provinces in the specified regions, collected between 2012 and 2014 at intervals of 1 and 10 min, were analyzed using regression and correlation methods along with a specialized algorithm for classifying days based on clear sky index terms. The statistical analysis identified days with significant potential for energy accessibility, exceeding 50% of the average. The findings suggest a correlation coefficient of approximately 0.30 for energy and non-linear regression with clear sky index coefficients around 0.80. The method employed demonstrated accuracy when compared to theoretical simulations of the clear sky index in the region, indicating its potential applicability in other regions of interest.

Keywords: clear sky index; accessibility; spatial; regression; solar energy

Citation: Mucomole, F.V.; Silva, C.A.S.; Magaia, L.L. Regressive and Spatio-Temporal Accessibility of Variability in Solar Energy on a Short Scale Measurement in the Southern and Mid Region of Mozambique. *Energies* **2024**, *17*, 2613. https://doi.org/10.3390/en17112613

Academic Editor: Manolis Souliotis

Received: 21 January 2024
Revised: 7 March 2024
Accepted: 8 March 2024
Published: 29 May 2024

1. Introduction

The blackbody radiation curve, which represents the solar radiation spectrum, undergoes a shift towards lower intensities and longer wavelengths as the temperature decreases [1,2]. However, the solar energy that reaches the Earth's surface is slightly diminished and can vary in certain regions [3] due to factors such as dispersion caused by solid particles, dust, aerosols, and gases present in the atmosphere (among others) [2,4,5]. Societies are constantly evolving and growing, resulting in increased energy consumption to meet daily needs [2]. For instance, in 2023, the global population was estimated to be 18.01 million people [6]. Unfortunately, not everyone has access to energy [2], although the number of unserved individuals decreased from 1.2 billion to 733 million between 2010 and 2020 [6,7], resulting in an increase in accessibility from 83 to 91% [2]. To accelerate global electrification by 2030, compensating for the slowdown observed between 2010 and 2018, as well as between 2018 and 2020 [6,8], it is necessary to increase the number of new connections to 100 million per year [2]. However, at the current rate, this target will only be achieved by 92% [2,7]. Therefore, it is crucial to promote renewable actions on a large scale,

aiming for more than 30% of energy generation to come from renewable sources (net zero emissions by 2050), while reducing reliance on fossil fuels [6,7,9]. It is worth noting that approximately 80% of the global population without access to electricity resides in rural areas, while urban areas have achieved a stable access rate of 97% since 2016 [2,7]. Notably, urban electrification has experienced faster growth in Sub-Saharan Africa compared to other regions, with an annual growth rate of 1 percentage point between 2010 and 2020 [2,6–8]. The 20 countries with the largest access deficits are home to approximately 76% of the total population (Sub-Saharan Africa, Central Asia, South Asia, East Asia, South-East Asia, West Asia, and North Asia), with Nigeria, the Democratic Republic of the Congo, and Ethiopia having around 92 million, 72 million, and 56 million people, respectively, without access to electricity [6,7]. Mozambique, with approximately 20 million people lacking access to electricity, ranks 6th [2,6,7].

In Mozambique, specifically in the eastern channel, southern region, mid region, and part of northern Mozambique, existing systems face challenges due to the variability in photovoltaic energy production [2]. Understanding the spatiotemporal variability in irradiance is crucial for effectively integrating a growing number of photovoltaic power systems [10]. Electricity of Mozambique (EDM) projected a PV capacity of 53 MW at the beginning of 2024, with an anticipated increase to 55 MW by the end of the year and further expansion in the future to meet the projected global demand of 800 GW by 2050, aiming to reduce environmental pollution [2,7]. The eastern channel of Mozambique, encompassing the southern and mid regions, currently has a total PV capacity of 119 MW (including autonomous PV systems and grid-connected ones), and is facing challenges due to solar energy variability affecting PV system performance and battery storage sizing. Variability in solar radiation has significant impacts on photovoltaic system efficiency and battery storage sizing, as well as on the balance between generation and load, and the maintenance of power quality, including voltage and frequency stability. It is essential to comprehend biases in the portrayal of temporal variability caused by temporally coarse-resolution observations, and also how spatial averaging (such as that from the distribution of photovoltaic power in a region) reduces variability. Understanding the spatiotemporal volatility of irradiance fields and their increments is crucial for the planning and dependable operation of upcoming electrical networks and their related subsystems [10]. Recent research has focused on analyzing solar energy from an on-site perspective. This involves studying Global Horizontal Irradiance (GHI) samples collected locally or through remote sensing using satellites. The purpose of this analysis is to understand the trajectory, spatial distribution, and temporal behavior of solar energy. One specific application of this analysis is in the dimensioning of photovoltaic systems. In 2015, the dimensioning analysis of photovoltaic systems followed. It was observed that the already installed and designed systems exhibited instability and fell short of the expected lifetime [2,11]. This can be attributed to a lack of knowledge regarding periods with varying amounts of solar energy. It is crucial to consider these periods when designing solar systems, whether they are autonomous or connected to the electrical grid. By understanding the periods of high solar energy incidence, excess energy can be utilized for other purposes. Similarly, during periods of low solar energy, the system can be designed to ensure that energy supply is not compromised. This is important to prevent any wastage or strain on the photovoltaic system devices, which are susceptible to the variability in solar energy. In a recent study, the variability in PV energy output was quantified. It was found that the total number of PV systems determines the output, and this variability was measured as 1 [12,13]. Additionally, the spatio-temporal variability in PV system networks was analyzed. It was demonstrated that classifying the sky conditions into different categories, such as intermediate sky, increases the likelihood of fluctuations in solar energy production and system output [10,14,15]. To further evaluate the behavior of solar energy, the clearness index K_t was assessed using on-site measurements of GHI. The correlation was studied over a time interval ranging from 1 to 24 h. The evaluation revealed that the daily GHI exhibited various local sky conditions, with clear and cloudy skies being the predominant

types [16–18]. Certain assessments involve computational estimations utilizing proactive inference techniques of GHI data on a flat surface with an optimal tilt angle at 5 min intervals. It has been noted that there is a fluctuation in solar energy classification on tilted surfaces [19–21]. Another assessment conducted on flat surfaces involved the ability to adjust certain parameters in the evaluation algorithm using a GHI sample obtained through traditional instruments on-site. This assessment revealed the temporal fluctuations in solar energy, specifically in the southern region of Mozambique, where the data were collected at intervals ranging from 1 to 10 min during a measurement campaign. The results indicated a prevalence of clear and partially cloudy days, with a smaller occurrence of cloudy skies [2,22–24]. Additionally, there is a growing trend to manage the output of solar photovoltaic energy by forecasting PV production through GHI processing for renewable energy management. This helps to understand the variability in solar resources and confirms the presence of fluctuations in terms of high-frequency changes in solar energy density [25,26]. However, despite the utilization of sample data, particularly from GHI, to study the dispersion of solar energy and its spatial and temporal behavior, there is a higher margin of error when inferring data from satellite-extracted samples compared to on-site measurements. The error is approximately 0.55 for satellite inference compared to 0.50 for on-site data inference [1,2]. This discrepancy can be attributed to various factors, including reduced content in satellite data collection, partial absorption during satellite inference, and atmospheric influences that affect the accuracy of satellite-mediated sample data. Furthermore, satellite data collection platforms primarily provide data in hourly, daily, weekly, monthly, and/or annual averages [27,28], which limits the accuracy of assessing real-time solar energy variability on a shorter time scale. Furthermore, the cost of conducting a localized data inference campaign using traditional radiometers installed on the Earth's surface to collect and analyze radiation and its components is still prohibitively high.

However, recent studies have demonstrated the effectiveness of utilizing satellite data to predict short-term variability in global horizontal irradiance (GHI) and observed solar energy variability. The potential of satellite-derived GHI for accurate photovoltaic (PV) predictions was highlighted [29–33]. In addition, the assessment of solar energy adoption in agricultural practices has been explored. This analysis involved gathering local perceptions and samples of GHI to evaluate the significance of solar energy in achieving higher returns [34]. Moreover, the analysis of urban morphology indicators for on-site solar energy assessment has been conducted. These findings indicate a strong correlation (R^2 = 0.91) between the gross space index, facade-site relationship, sky factor, and solar irradiance, suggesting the potential for utilizing these indicators in solar energy analysis within urban contexts [35–37]. A probabilistic solar energy forecast was generated using multiple linear regression analysis, based on data from various renewable energy sources. This forecast serves as a valuable resource for mitigating the challenges posed by the uncertain variability in solar PV and renewable energy in general [38–40]. The prediction of solar radiation fluxes for solar PV systems was achieved through the use of in situ GHI, multiple regression, and correlation analysis. The results indicate that the mean error values fall within acceptable margins, supporting the use of global solar radiation flux for design and performance estimation in solar applications [41–43]. Additionally, the model employed in this study is applicable in areas without meteorological stations [42]. Various studies have successfully modeled GHI for any location on Earth using regression analysis and high-resolution GHI data [42–45]. These studies demonstrate improved performance and reliability in simulating real variability at specific sites. Linear regression analysis was employed to characterize the solar radiation based on in situ data collected from different locations [42]. The analysis revealed that the incorporation of Hay effects did not reduce the dispersion in the regression parameters. Upon reviewing the information provided, it is imperative to analyze solar energy not only through a regressive lens, but using multiple data sources to comprehend its behavior and intensity. Additionally, examining the measurement of accessibility in both space and time, along with its regression in long-

term assessment, is crucial for gaining insight into the real access and functionality of solar energy. This understanding is essential for the development of reliable photovoltaic systems with high power output, durability, and stability, unaffected by network fluctuations or changes in solar irradiance.

Mozambique stands out as a region abundant in solar energy [2], yet approximately 55% of its central population lacks access to efficient electrification. By studying the correlative and regressive patterns of solar energy in this area, there is potential for significant advancements in the installation of highly efficient plants. This knowledge can lead to the replacement of outdated or poorly designed systems, ultimately improving the lifespan and effectiveness of existing solar energy setups.

Within the framework of the National Energy Fund of Mozambique (FUNAE), the researcher utilized data collected from approximately eight measurement stations to investigate the regression and spatial-temporal variability in solar energy availability in the southern and mid region of Mozambique. The data were collected over a time span ranging from 1 to 10 min. To evaluate the sample, an algorithm was developed that considered the inferred GHI (Global Horizontal Irradiance) at each station. Additionally, a mechanism was devised to assess the reliability of solar energy evaluation and quantify it in specific portions, which provided a measure of the correlation dispersion between stations at interprovincial distances. This mechanism also indicated the measure of rule coefficients between stations. Furthermore, a classification scheme was implemented to identify different types of skies and quantify the number of days associated with each type. Systematic correlation statistics were conducted to analyze the temporal variability in these different types of days. Correlations between increments of two sensor points and large spatial averages were also examined. These analyses aimed to establish the accessibility of regression and spatial-temporal solar energy availability in the southern and eastern channel region of Mozambique, both on a short-term measurement scale and a long-term data recording scale. The findings from this research will contribute to the improved projection of projects utilizing solar PV energy in the region. Additionally, a consultation tool for solar radiation in the central-western region of Mozambique will be developed.

The results obtained establish a set of procedural steps that can be applied globally, while allowing for the adaptation of local input variables to the specific region, such as topography, climate, and local incidents. However, it can be demonstrated that within the study area, energy flows from Nhamadzi, Barue–1, and Barue–2 to Chipera along the investigation path. Furthermore, based on more consistent measurements taken during annual observations in 2012, it is evident that the Nhamadzi and Chipera stations have the highest potential for full solar radiation availability on suitable days, followed by the Barue–2 and Barue–1 stations, all of which exceed 50% in each instance.

2. Materials and Methods

2.1. Data Collection and Processing

The GHI data sample was collected during the solar radiation measurement campaign conducted by the National Energy Fund of Mozambique (FUNAE) between 2012 and 2014. The campaign took place in the south and mid region of Mozambique, specifically in the provinces of Maputo, Gaza, Inhambane, Sofala, Manica, and Tete. The data were collected at three different locations: Maputo–1, Ndindiza, Massangena, Pembe, Nhamadzi, Barue (Barue–1 and Barue–2), and Chipera. In Maputo–1, Ndindiza, Massangena, Pembe, Nhamadzi, and Chipera there was one station each, while in Barue there were two stations installed at the same latitude. Overall, there were four high-resolution radiometers placed at distances $d_{ij} > 1000$ km.

Figure 1 illustrates the correlation and interconnection between the stations in the south and mid region and other measurement stations strategically located throughout Mozambique. It shows the relationship between the distance from the south and from the mid region, resulting in a strong dependent relationship between the crossing from the south and the middle of country.

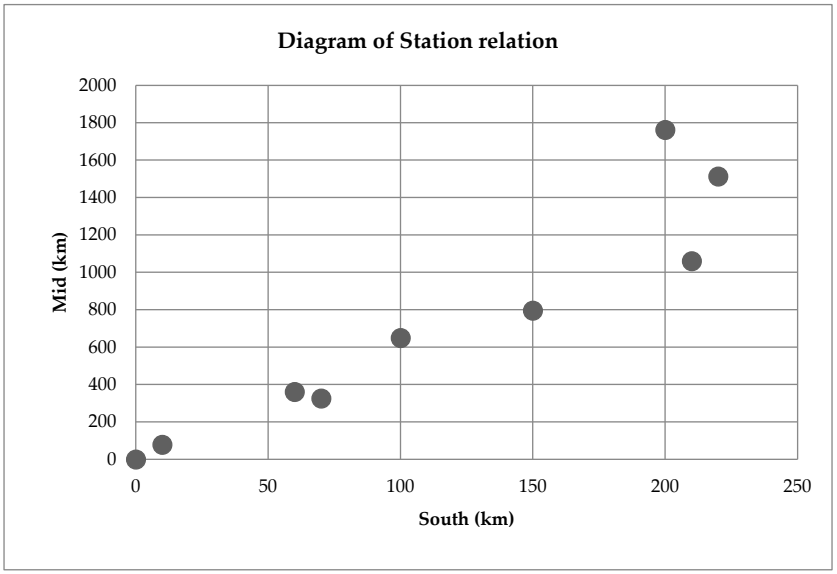

Figure 1. Map displaying the coordinates of the southern and mid regions for the combined station pairs.

Furthermore, Figure 1 illustrates that the density of repetition frequency for measuring stations in the channel-east region of Mozambique is greater for cutoff classes of 982.0 and 1094.0 km when taking into account the combination of sensor pair distances. The GHI radiation component and diffuse horizontal irradiation (DHI) were collected using Pyranometer radiometer sensors, as shown in Figure 2. These sensors were linked to a system that incorporated a Pyrheliometer to directly measure the direct normal irradiation (DNI) component.

Figure 2. Pyranometer used to measure GHI during the campaign.

The Pyrheliometer utilized for data collection underwent calibration to ensure the following optimal characteristics: a calibration factor ranging from 295 to 2800 nm, a spectral range with a 1 min response time, linearity within ±0.5% (0 to 1400 W/m^2), cosine accuracy of ±1% ($0 < Z < 70°$) and ±3% ($70 \leq Z < 80°$), and temperature response accuracy of ±1% from −20 °C to 40 °C. Data collection was conducted using a Campbell–23X data logger, version No. 0021, Model 4280, set to operate at a frequency of 1 Hz, with the storage of the instantaneous average of 1 and 10 min intervals.

For the duration of the measurement period, each instrument underwent regular seasonal maintenance. This maintenance included various tasks such as transferring data,

replacing batteries, cleaning, adjusting, leveling, and realigning. Throughout this process, the cleaning and orientation periods were meticulously recorded and recognized as periods of interference and turbulence during the data selection phase. In the event of a data miscalibration, the voltage angle was promptly identified, although such instances were rare during the week-long campaign.

Afterwards, a comprehensive quality control procedure was conducted on the data to eliminate any erroneous values. Subsequently, the data underwent processing using specialized software specifically designed for radiation calculation, with a time interval of 1 and 10 min.

The processing of the data is illustrated in Figure 3, which demonstrates the categorization of the data into two groups: acceptable days and unacceptable days. Acceptable days are those in which the experimental GHI spectrum closely aligns with the calculated theoretical radiation spectrum. Conversely, unacceptable days are characterized by a significant deviation between the experimental GHI spectrum and the calculated theoretical irradiation, either being considerably lower or excessively higher. This deviation is attributed to various atmospheric factors, such as intense cloud reflection and inhibitors that impede the passage of solar radiation, thereby impacting the accurate determination of incident radiation.

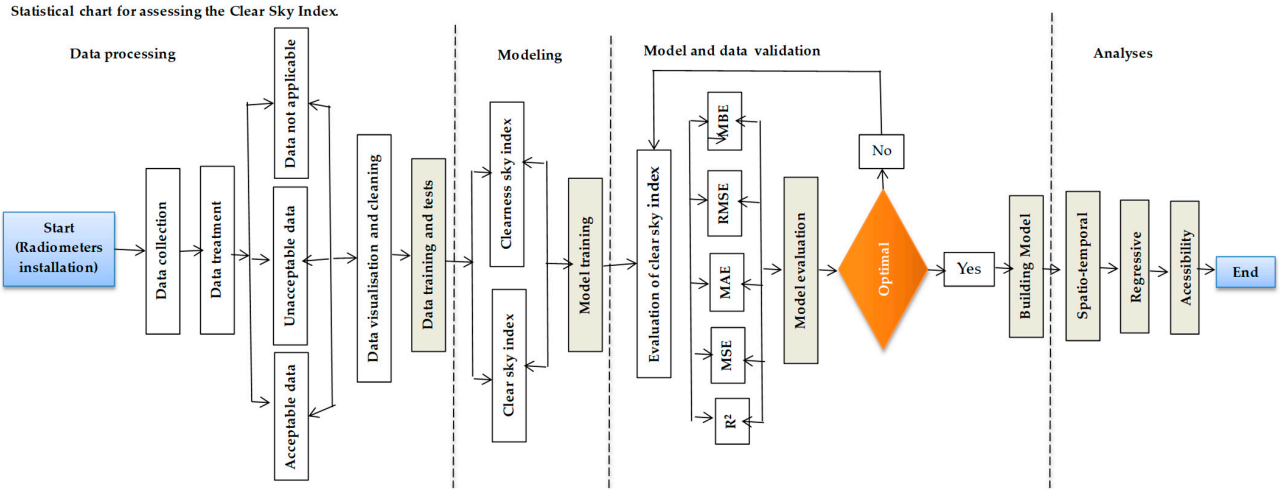

Figure 3. Statistical design research framework diagram.

Furthermore, there exist days when the data sample is not applicable, as it only accounts for around 25% of the daily measurements or lacks any recorded measurements. This situation arises due to various factors such as the unavailability of electrical power to the measurement system, the presence of animals, or the presence of fixed obstacles that hinder and obstruct radiation inference during that specific time frame. By implementing this approach, the occurrence of outliers is reduced, leading to an improved statistical analysis and the categorization of days into distinct groups.

Following the examination of the raw GHI sample, several tests were conducted to determine the K_t^*. The clear sky index exhibited excellent values, aligning closely with the theoretical light sky irradiation spectrum, making it an ideal choice. The data for the K_t^* underwent analysis using various techniques for inferring measurement errors. Once again, the K_t^* data were visualized, along with their daily behavior. Ultimately, the model's conceptualization led to the determination of an increment in the clear sky index (ΔK_t^*). Finally, spatial and temporal meta-analyses of K_t^* were performed to assess the accessibility of solar energy in the study region.

2.2. Study Area

The research area, which is situated in the south and mid region of Mozambique, spans between the 10°27′ and 26°52′ south latitude parallels and the 30°12 and 40°51′

east longitude meridians. Within this region, eight stations, namely Maputo–1, Ndindiza, Massangena, Pembe, Chipera, Nhamadzi, and Barue, have been established. Table 1 provides detailed information about the latitude and longitude of these stations.

Table 1. Location of study stations.

ID	Name	Number of Stations	Province	Longitude	Latitude
MZ06	MZ06–Chipera	1	Tete	31°40′3.4″ E	14°58′28.1″ S
MZ11	MZ11–Nhamadzi	1	Sofala	35°2′18.7″ E	19°43′46.6″ S
MZ15	MZ15–Massangena	1	Gaza	32°56′26.7″ E	21°34′59.5″ S
MZ17	MZ17–Ndindiza	1	Gaza	33°25′22.8″ E	23°27′37.1″ S
MZ20	MZ20–Pembe	1	Inhambane	35°35′35.5″ E	22°56′44.3″ S
MZ21	MZ21–Barue	2	Manica	33°13′0.8″ E	17°47′32.5″ S
MZF01	MZF01–Maputo–1	1	Maputo City	32°9′39.8″ E	23°55′7.8″ S

Figure 4 displays the topographic profile of the south, mid region, highlighting the various measuring stations. The purpose of preparing the sample was to perform calculations using data collected between the time the sun rises and sets. The sample was obtained from the FUNAE campaign, specifically from Maputo–1–Maputo City, Ndindiza–Gaza, Massangena–Gaza, Pembe–Inhambane, Nhamadzi–Sofala, Barue–Manica, and station Chipera–Tete. The sample consists of three years of complete measurement data from 2012, 2013, and 2014, starting from the sixth month of each year. Therefore, the data only cover the months from June to December. In 2013 and 2014, the data include measurements for all months of the year. In total, there are approximately 315,360.0 daily radiation data points in the useful area.

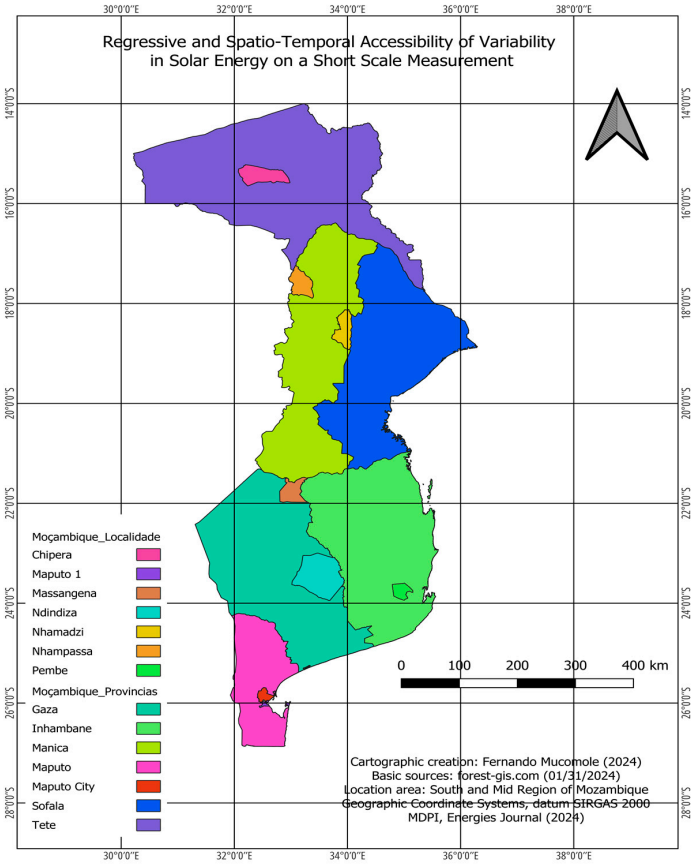

Figure 4. Study area section: south and mid region size of the Mozambique sample.

During certain months, there may be fluctuations in the data, such as missing values for a specific period or half of the month. To address this, a priori classification was necessary.

An example of this classification can be seen in Figure 5, which shows the process of selecting days for an applicable case at the Barue−1 station in 2013. This process was carried out among all four stations whose data samples were analyzed.

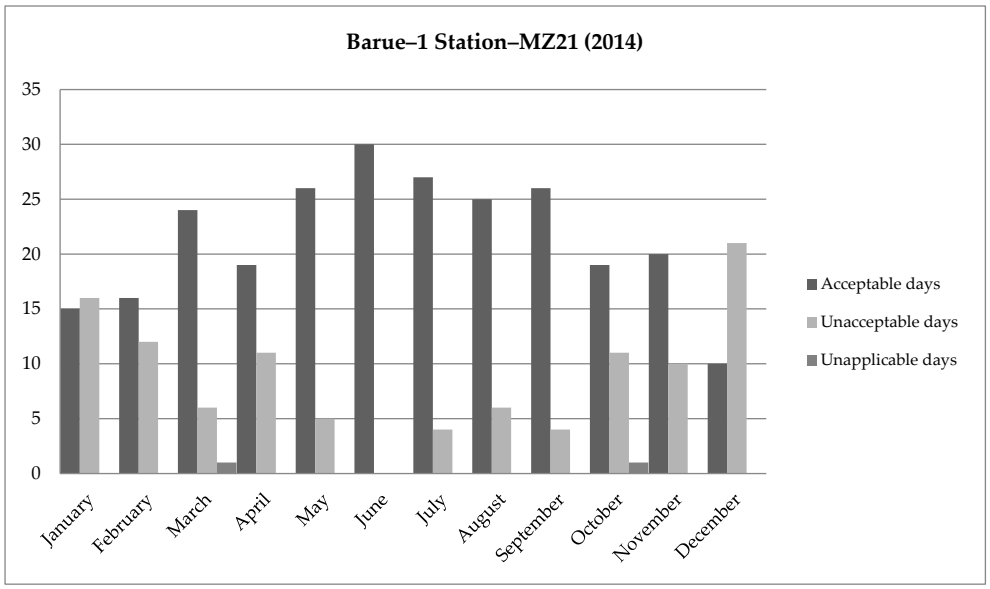

Figure 5. Choosing dates at the Barue–1 station for the year 2014.

2.3. Experimental Procedure

Solar radiation fluctuates during the day, influencing the daily and annual evaluations of solar energy on the Earth's surface. The equation of time and the distance from the standard meridian are measured in minutes, offering a precise representation of energy distribution throughout the seasons. This correlation is illustrated by Equation (1), with the time equation variable E indicating the 60 min variation between summer and standard time [1,46].

$$E = 229.2 \times (0.000075 + 0.001868 \times \cos(B) - 0.032077 \times \sin(B) - 0.014615 \times (2 \times \cos(B)) - 0.04089 \times (2 \times \sin(B))) \quad (1)$$

The number of days in a given year, denoted as n, varies between 1 and 365. In Equation (1), the parameter B is determined by the formula $B = (n - 1) \times (360/365)$ [16]. It is crucial to consider the solar angle coordinates when analyzing the sun's position at a specific time of the day. To compute the direct normal irradiance (DNI) under clear sky conditions at an altitude above 2.5 km, Equation (2) can be used to relate the incoming radiation to the measurement on the horizontal surface of the earth [1,2,47].

$$G_{cnb} = G_{on}\tau_b \quad (2)$$

Equation (2) defines G_{on} as the extraterrestrial radiation received by a plane perpendicular to the radiation on a given day, as stated in Equation (3) [27,28].

$$G_{on} = G_{sc}\left(1 + 0.0033\cos\left(\frac{360n}{365}\right)\right) \quad (3)$$

The evaluation of the daily radiation's efficacy was conducted by calculating the standard direct horizontal radiation. This measurement is derived from the sum of direct horizontal radiation received from clear skies, showcasing the potential fluctuations throughout the day as denoted by Equation (4) [16]. By transforming the correlation of

Equation (4), it is possible to depict the direct radiation instead of the currently analyzed direct radiation [1,2].

$$I_{cb} = I_{on}\tau_b \cos\theta_z \tag{4}$$

I_{on} represents the extraterrestrial radiation incident on a regular plane, while τ_b denotes the atmospheric transmittance for the incident radiation, and θ_Z represents the zenith angle [48].

It has been observed that the presence of GHI is reduced during sunrise and sunset. Nevertheless, there is a notable surge in the occurrence of solar energy during the peak period.

The analyzed days are within the range of theoretical radiation distribution under clear skies, conforming to a Gaussian curve. To link GHI with clear sky radiation, the clear sky index K_t^* was introduced. This index signifies the correlation between GHI and theoretical radiation under clear skies, which pertains to the irradiation from the Earth's atmosphere on cloudless days [32], as shown in Equation (5) [2,49].

$$K_t^* = \frac{GHI}{G_{Clear}} \tag{5}$$

G_{Clear} is the total radiation received on a horizontal surface, which includes both direct and diffuse radiation within an hour. The average value was determined using the GHI measurement interval of one day (amplitude) with M measurement intervals to categorize various sky types, as described in Equation (6) [1,47,50].

$$\overline{K_i^*} = \frac{1}{M}\sum_{t=1}^{M} K_t^*(t) \tag{6}$$

Figure 6 illustrates the flawless progression of the daily course, perfectly matching the theoretical frequency density and frequency of the clear sky index averages derived from Equation (6). This demonstrates an ideal representation of the experimental treatment, sample selection, and the utilized clear sky index algorithm [2,51].

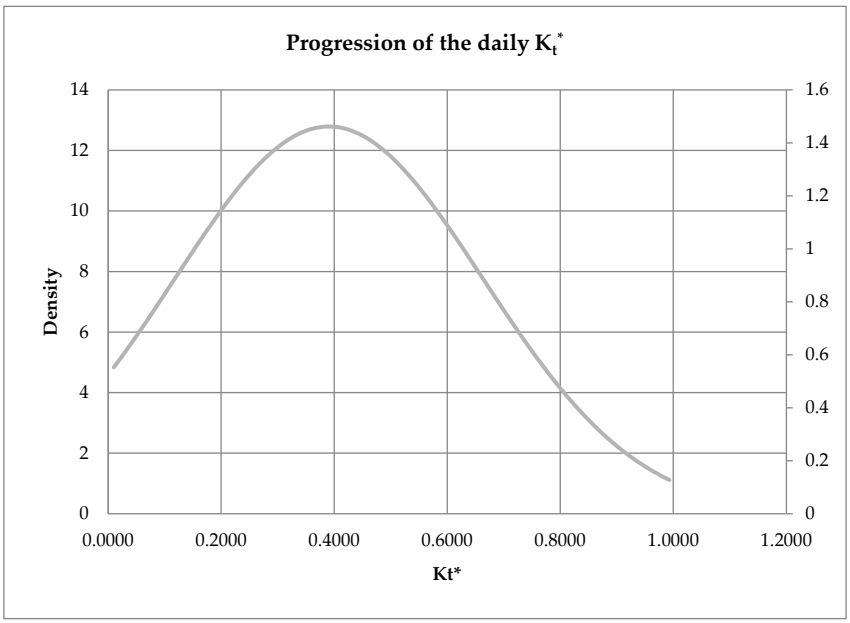

Figure 6. Progression of the daily K_t^* values over time.

To assess the fluctuations in temporal variability, a metric is employed to compute the disparity between the present and preceding clear sky index values [27,50]. To guar-

antee precise outcomes, a time interval of ten minutes was incorporated to discern the dissimilarity between two consecutive measurements, as depicted in Equation (7) [13,49].

$$\Delta K_t^* = K_{t+1}^* - K_t^* \tag{7}$$

The statistical software produced different outcomes when adjusting the modeled K_t^* values, however, it successfully enhanced the accuracy of the analysis and RMSE (Root Mean Squared Error), with a 30% margin of error. The nominal variance was evaluated by computing the standard deviation of K_t^* and ΔK_t^* as depicted in Equation (8) [2,52,53].

$$\sigma(\Delta K_t^*) = \sqrt{var\left[\Delta K_{t\,\Delta t}^*\right]} \tag{8}$$

The GHI and Total Theoretical Radiation spectra were employed chronologically to detect a maximum of 10 days in which GHI closely corresponded to Total Theoretical Radiation, signifying satisfactory performance. Likewise, the same approach was used to identify unsatisfactory days. The probability density function $f(x)$ was determined using the Kernel Density estimation function (PDF) [2].

The days selected for each month were arranged in a table that included the day reference, the average value of K_t^*, σK_t^*, and $f(x)$.

Subsequently, the graphical representation of the spectrum of K_t^* was plotted against σK_t^*, $\overline{K_t^*}$, and $f(x)$. This allowed for the calculation of the average values of ΔK_t^*. By analyzing the graphs, the sample was categorized into different classes. Cloudy days were identified as those with horizontal and vertical coordinates falling within the range before the average of K_t^* and below σK_t^*. Clear sky days were defined as those with coordinates falling within the range after the average of K_t^* and below σK_t^*. Lastly, intermediate sky days were defined as those with coordinates above the σK_t^* values, regardless of the K_t^* values, as shown in Figure 7.

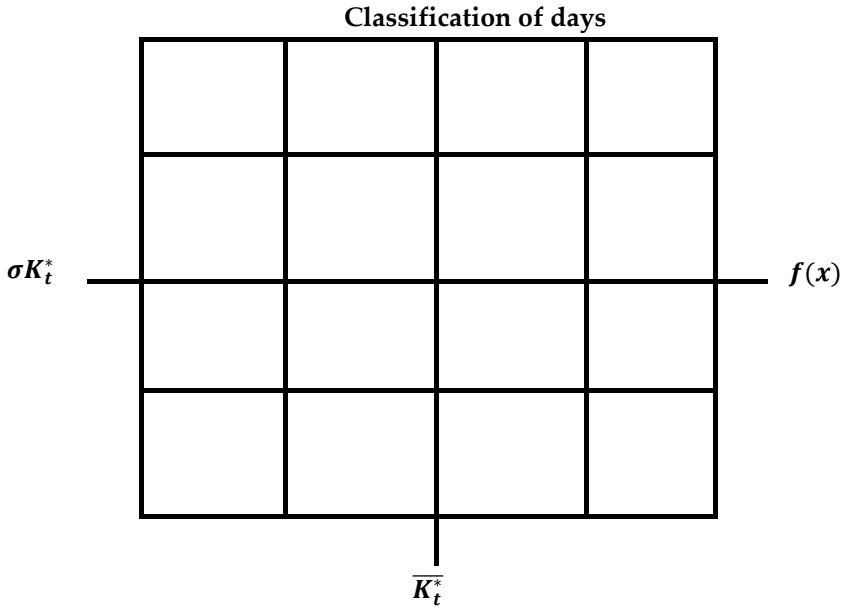

Figure 7. Classification of the days of each month of the year, using average values of K_t^*, σK_t^*, and $f(x)$.

New spectra were generated by tallying and analyzing various types of days, such as clear, cloudy, and intermediate. These spectra were then displayed in a bar graph. The main objective of this analysis was to determine the month with the highest occurrence of clear and cloudy days. The values of ΔK_t^* were recorded for each day classification. Following this, frequency density histograms were produced to depict the distribution of ΔK_t^* values across the three categories of days. By examining these histograms, the variability of specific days was evaluated for each day throughout the chosen year.

To observe the accumulation of days across all classes simultaneously, histograms were created. These histograms plotted the variation of K_t^* against frequency density for each type of day in each year. Different values of K_t^* were examined for different types of days (clear, intermediate, and cloudy), establishing a connection based on the correlation coefficient distance or systematic relationship of the clear sky index $\rho_{ij}^{\Delta K_t^*}$, as presented in Equation (9) [10,54].

$$\rho_{ij}^{\Delta k_t^*} = \frac{cov\left(\Delta K_{t,i}^*(t), \Delta K_{t,j}^*(t)\right)}{\sigma_{\Delta K_{t,i}^*(t)} \sigma_{\Delta K_{t,j}^*}} \tag{9}$$

The increments and corresponding arithmetic averages of the time series between two locations i and j, denoted as $\Delta K_{t,i}^*(t)$, $\Delta K_t^*, j(t)$ and $\overline{\Delta K_{t,i}^*}$, $\overline{\Delta K_{t,j}^*}$, respectively, were analyzed [2,49].

Statistically, the inequality $-1 \leq \rho_{ij}^{K_t^*} \leq 1$ holds true. Spatially, when considering a subspace station located between two points x and y, the randomized values related to $x + y$ can be expressed as $\sigma_{x+y} = \sqrt{\sigma_x^2 + \sigma_y^2 + 2\chi_{xy}\sigma_x\sigma_y}$. It is important to note that $\sigma_{\Delta k_{t,i}^*(t)} \neq 0$ and $\sigma_{\Delta k_{t,j}^*} \neq 0$ [54,55].

The difference in points between the two sets of measurements was denoted as t. Likewise, the relationship or consistent link between the changes in the clear sky index $\rho_{ij}^{\Delta k_t^*}$ was examined [2,15].

The correlation study involved two equidistant measuring stations, starting from the Maputo–1 station and continuing to the Ndindiza, Massangena, Pembe, Barue–1, Barue–2 stations, with the evaluation endpoint being the Chipera station, from FUNAE's GHI measurement campaign [56]. The systematic correlation of clear sky index increments was assessed through the systematic correlation connection $\rho_{ij}^{\Delta K_t^*}$.

Initially, this comparison was made with the spatial correlation coefficient model proposed by Marcos et al. (2011) [52] and Barry et al. (2017) [57].

$$\rho_{ij}^{\Delta K_t^*} = exp\left(\frac{t^{-1} d_{ij} ln(0.2)}{1.5}\right) \tag{10}$$

In the study region, the spatial correlation coefficient model suggested by Hoff and Perez (2012) [12] was employed, incorporating a range of relative cloud speed values between 4 m/s and 6 m/s.

$$\rho^{\Delta k_t^*} = \left(1 + \frac{d_{ij}}{t.v}\right)^{-1} \tag{11}$$

Furthermore, within the study area, the spatial correlation coefficient model proposed by Duffie & Beckman (1991) [1] was also employed. This model has the capability to accurately depict the decorrelation curves for various frequencies, based on either predetermined or specified values of k_t^*. This relationship is defined in Equation (12) [1].

$$\rho^{\Delta k_t^*} = \frac{exp\left(\gamma \Delta k_{t,\,min}^*\right) - exp(\gamma \Delta k_t^*)}{exp\left(\gamma \Delta k_{t,\,min}^*\right) - exp\left(\gamma \Delta k_{t,\,max}^*\right)} \tag{12}$$

The parameter γ is employed for explicit correlation curve fitting. The examination focused on the accessibility of solar energy, analyzing the distribution patterns throughout the year and classifying the number of days as acceptable, unacceptable, or non-applicable, based on the relationship described in Equation (13) [1,16,27].

$$K_t^* = \frac{1}{G_{clear\,i}} \left(\sum_{i=1}^{n} DNI_i + \sum_{i=1}^{n} DHI_i\right) \tag{13}$$

Over the years, the data measurement has consistently yielded exceptional data with minimal imperfections. Particularly, the year 2012 stood out across all aspects, producing remarkable outcomes.

A quantitative chart was formulated to depict the highest percentage and the most favorable days, which were distinguished by clear skies and frequent incidents. Furthermore, by examining the peak of the probability density function derived from the kernel density estimation for each day within the designated study area, the cloudiest day was identified.

The determination of the average area's variability and its changes, which were based on the average area A, were assessed by employing random circle sampling in the southern and mid regions of the east-channel of Mozambique. This evaluation was conducted using Equation (14) [2,47].

$$\hat{\sigma}^{\Delta k^*} = \frac{\sigma_{area}^{\Delta K_t^*}}{\sigma_0^{\Delta K_t^*}} \tag{14}$$

where, $\hat{\sigma}^{\Delta k^*}$ represents the normalized standard deviation of the clear sky index increment, which may originate from the initial clear sky index; $\sigma_{area}^{\Delta K_t^*}$ denotes the standard deviation of the clear sky index increase within the research area, while $\sigma_0^{\Delta K_t^*}$ stands for the standard deviation of normalization over a one-minute time interval [10]. The normalized values of the average area quantities' variability, in relation to the standard deviation, were employed to evaluate their significance and any alterations.

Finally, the analysis of solar energy accessibility in the central-eastern region of Mozambique was conducted, focusing on the applicability of various methods in comparison to linear regression. The regression matrix and other factors were considered in this assessment, given in Equation (15) [58,59].

$$Y = \begin{bmatrix} Y_1 \\ Y_2 \\ Y_3 \\ \cdots \\ Y_n \end{bmatrix} \tag{15}$$

Y has dimensions of $n \times 1$ [60]

$$X = \begin{bmatrix} X_{11} & X_{12} & X_{1z} \\ X_{21} & X_{22} & X_{2z} \\ \cdots & \cdots & \cdots \\ X_{n1} & X_{n2} & X_{nz} \end{bmatrix} \tag{16}$$

while X has dimensions of $n \times z + 1$ [58].

$$\beta = \begin{bmatrix} \beta_0 \\ \beta_1 \\ \cdots \\ \beta_z \end{bmatrix} \tag{17}$$

There are α and p explanatory variables, β is a matrix of size $z + n \times 1$ of explanatory variables with β_0 constants, α and ε are matrices of $n \times 1$ residuals [61,62].

$$\varepsilon = \begin{bmatrix} \varepsilon_0 \\ \varepsilon^1 \\ \cdots \\ \varepsilon_z \end{bmatrix} \tag{18}$$

The computerization for analysis in terms of logarithmic regression observed the existence of a trend of a greater deviation of pairs of stations for other types of regression models [63].

3. Results

3.1. Occurrence Content and Categorization of Varieties of Days

In the process of classifying acceptable days, as illustrated in Figure 8, for Nhamadzi and Barue–1 stations in 2012, there is a greater focus on the maximum values of K_t^* during the hot season and the minimum values during the cold season. This is in contrast to what is observed on unacceptable days, as shown in Figure 9. Unacceptable days for the Nhamadzi station in 2012 and 2013 lack consistency in the timing of their measurements due to various influencing factors. It is essential to identify the days with the highest and lowest levels of radiation, as they play a crucial role in determining the success of both independent solar power systems and those connected to the conventional electrical grid. This information aids in sizing the system based on the availability of solar energy in the area. During periods of higher radiation, surplus energy can be generated and utilized for other purposes, such as injecting it into the electrical grid. The categorization of permissible and impermissible days plays a significant role in producing a well-structured ultimate evaluation. It discloses that Maputo–1 and Chipera stations encounter the most frequent instances of cloudless conditions, succeeded by Nhamadzi and Pembe. Lastly, Barue–2, Barue–1, Ndindiza, and Massangena each possess distinct attributes.

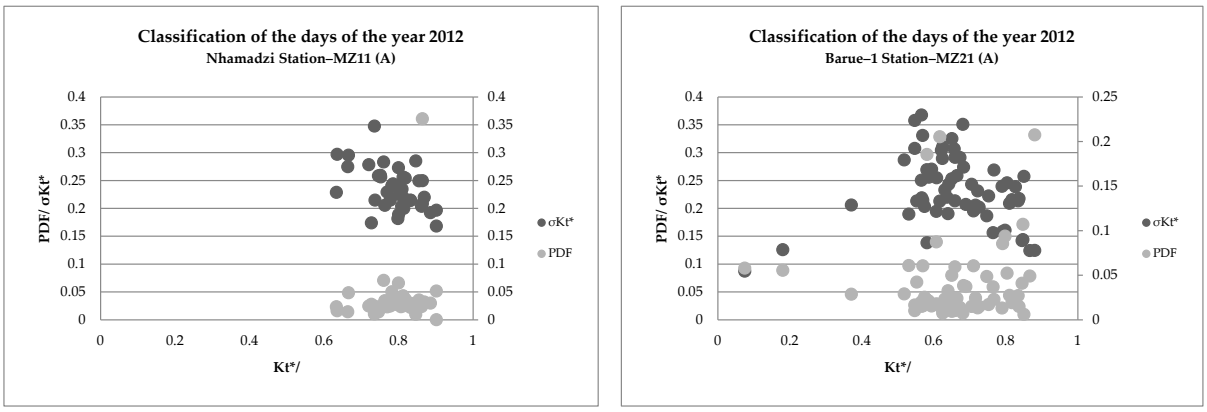

(**a**) (**b**)

Figure 8. Scatter diagram for classifying acceptable days for all months of the year, using the values of K_t^*, σK_t^*, and $f(x)$ for each day: Nhamadzi Station in 2012 (**a**) and Barue–1 Station in 2012 (**b**).

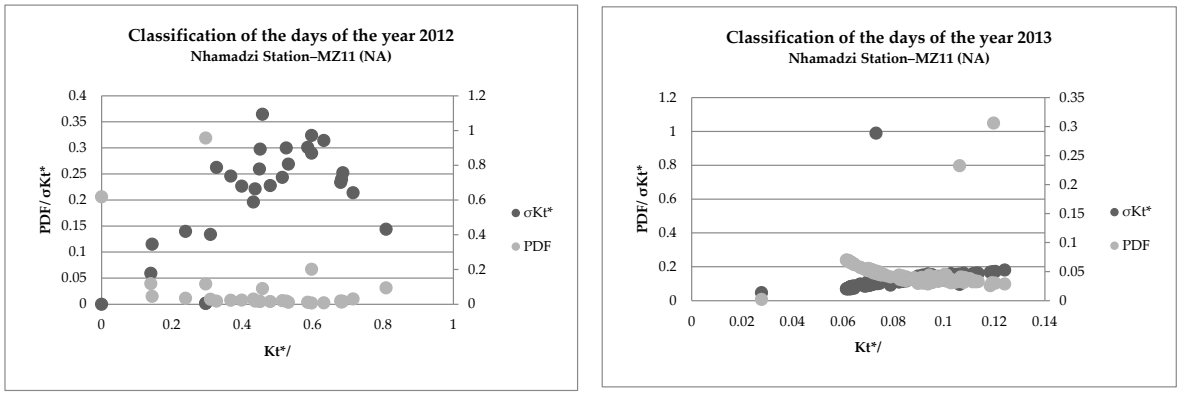

(**a**) (**b**)

Figure 9. Scatter diagram for classifying unacceptable days for all months of the year using the values of K_t^*, σK_t^*, and $f(x)$ for each day: Nhamadzi Station in 2012 (**a**) and in 2013 (**b**).

Chipera station in Tete: (1) The year 2012 saw acceptable days with varying K_t^* values, ranging from a minimum of 0.39 in July to a maximum of 0.99 in November. Cloudy days were limited to 0.82, while lower and upper intermediate sky days were restricted to 0.79 and 0.87, respectively. Clear sky days were limited to 0.94. On the other hand, unacceptable days in 2012 had K_t^* values ranging from 0.22 in August to 0.81 in September. Cloudy skies were limited to 0.45, lower and upper intermediate skies to 0.54 and 0.68, and clear skies to 0.79. (2) Moving on to 2013, acceptable days displayed a minimum K_t^* of 0.51 in June and a maximum of 0.82 in January. Cloudy days were limited to 0.63, while lower and upper intermediate skies were restricted to 0.67 and 0.74, respectively. Clear days were limited to 0.83. Unacceptable days in 2013 had a minimum K_t^* of 0.25 in May and a maximum of 0.76 in July. Cloudy skies were limited to 0.39, lower and upper intermediate skies to 0.51 and 0.64, and clear sky to 0.76. The Nhamadzi station in Sofala experienced varying levels of acceptable and unacceptable days in 2012, 2013, and 2014. In 2012, the minimum K_t^* was 0.64, observed in December, while the maximum was 0.92, also observed in December. Cloudy days were limited to 0.77, with lower and upper intermediate skies limited to 0.81 and 0.84, respectively. Clear days were limited to 0.91. Unacceptable days had a minimum K_t^* of 0.0001, observed in September and a maximum of 0.84, observed in October. Cloudy days were limited to 0.43, with lower intermediate skies at 0.46 and upper intermediate skies at 0.0001. Clear skies were limited to 0.82. In 2013, only unacceptable days were recorded, with a minimum K_t^* of 0.04 observed in December and a maximum of 0.14 observed in June. Cloudy days were limited to 0.08, with lower and upper intermediate skies at 0.09 and 0.11, respectively. Clear skies were limited to 0.14. Finally, in 2014, only unacceptable days were observed, with a minimum K_t^* of 0.07 in January and a maximum of 0.12 in May. Cloudy days were limited to 0.08, with lower and upper intermediate skies at 0.09 and 0.12, respectively, and clear skies at 0.12.

The Barue–1 station in Manica experienced varying levels of acceptable and unacceptable days from 2012 to 2014. In 2012, the minimum K_t^* value for acceptable days was 0.08 in December, while the maximum was 0.89 in July. Cloudy days were limited to 0.62, lower and upper intermediate sky days to 0.66 and 0.78, and clear sky days to 0.89. On the other hand, unacceptable days had a minimum K_t^* of 0.11 in October and a maximum of 0.71 in September. In 2013, the minimum K_t^* for acceptable days was 0.28 in October, with a maximum of 0.94 in August. Cloudy days were limited to 0.61, lower and upper intermediate days to 0.66 and 0.78, and clear days to 0.94. Unacceptable days had a minimum K_t^* value of 0.09 in September and a maximum of 0.93 in October. Finally, in 2014, the minimum K_t^* for acceptable days was 0.41 in December, with a maximum of 0.94 in April. Cloudy days were limited to 0.61, lower and upper intermediate skies to 0.68 and 0.76, and clear skies to 0.94. Unacceptable days had a minimum K_t^* of 0.16 in September and a maximum of 0.62 in October.

In Manica, the Barue–2 station recorded varying levels of acceptable and unacceptable days in the years 2012, 2013, and 2014. For instance, in 2012, the minimum K_t^* observed was 0.47 in September, while the maximum was 0.98 in November. Cloudy days were limited to 0.62, lower and upper intermediate skies to 0.69 and 0.75, and clear skies to 0.98 on acceptable days. Conversely, unacceptable days had a minimum K_t^* of 0.13 in October and a maximum of 0.67 in September. Cloudy days were limited to 0.41, lower and upper intermediate skies to 0.48 and 0.55, and clear skies to 0.67. The trends continued in 2013 and 2014 with varying K_t^* values and sky conditions on acceptable and unacceptable days.

Quantitative Analysis of Different Categories of Days

The percentage of acceptable days shown in Figure 10, and the percentage of unacceptable days also shown in Figure 11, indicates a higher quantity of clear and intermediate sky days, and a lower quantity of cloudy days. This enhances the presence of solar energy in the region for photovoltaic utilization as well as other purposes, quantified by the following proportions:

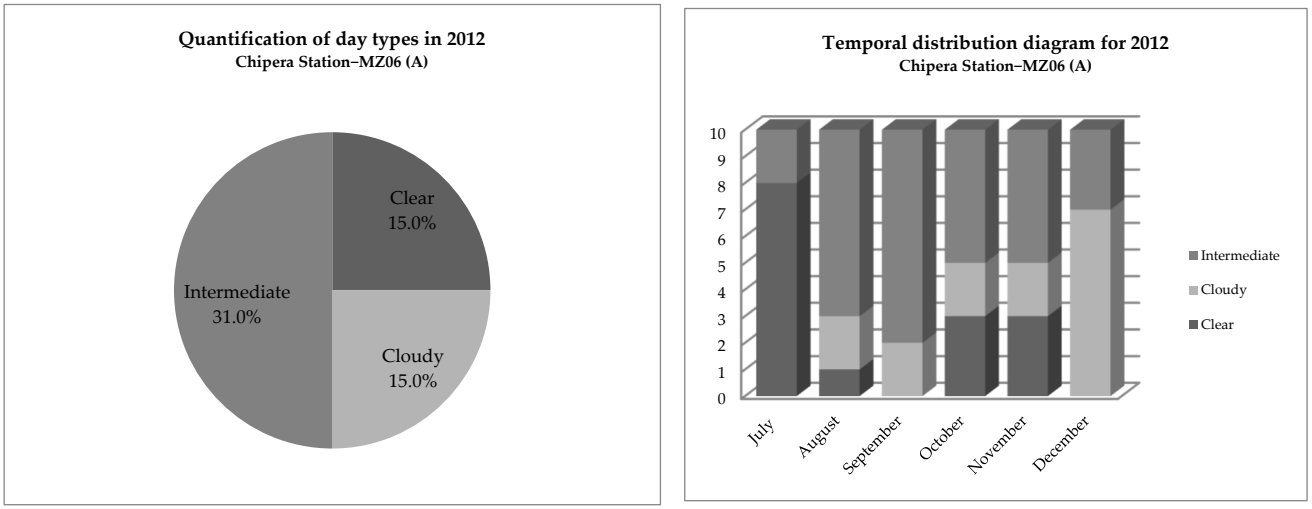

Figure 10. Quantification of day types and temporal distribution diagram for classifying the months' days, using the values of K_t^*, σK_t^*, and $f(x)$ for each day, at the Chipera Station in 2012.

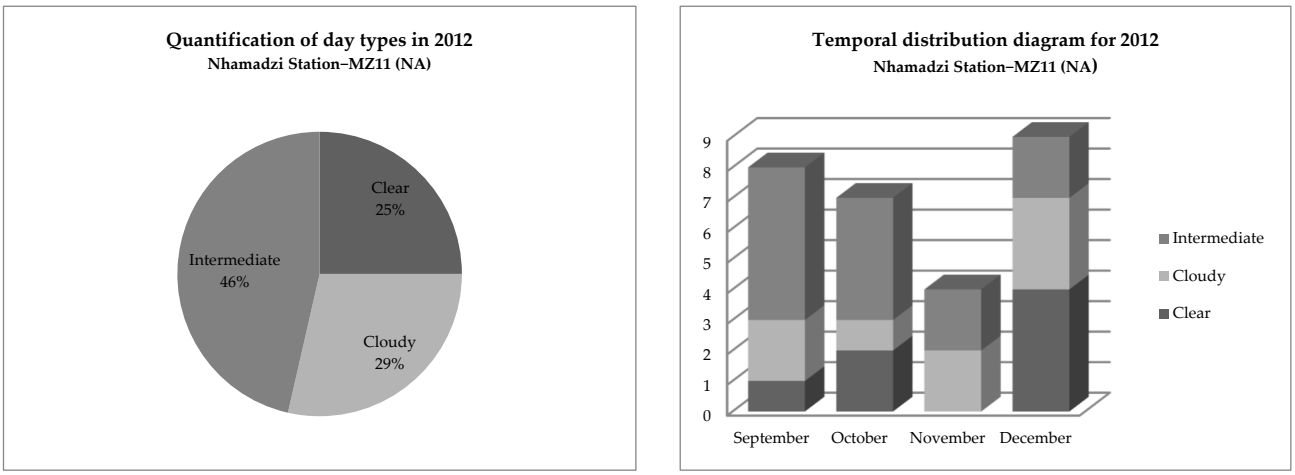

Figure 11. Quantification of types of unacceptable days and temporal distribution diagram for classifying day types of months, using the values of K_t^*, σK_t^*, and $f(x)$ for each day at the Nhamadzi Station in 2012.

At the Maputo–1 station in 2012, 53.0% of days were acceptable, with 13.0% clear, 11.0% cloudy, and 29.0% intermediate days. Of the unacceptable days, 49.0% were recorded, with 28.0% clear, 19.0% cloudy, and 28.0% intermediate days.

At the Pembe station in 2012, 68.0% of days were acceptable, with 19.0% clear, 18.0% cloudy, and 30.0% intermediate days. Of the unacceptable days, 41.0% were recorded, with 10.0% clear, 12.0% cloudy, and 21.0% intermediate days. These days are comparable for the days at the stations of Ndindiza and Massangena.

At the Nhamadzi station in 2012, 60.0% of days were acceptable, with 15.0% clear, 16.0% cloudy, and 28.0% intermediate days. Of the unacceptable days, 41.0% were recorded, with 10.0% clear, 12.0% cloudy, and 21.0% intermediate days. In 2013, no acceptable days were recorded. However, 100.0% of days were unacceptable, with 25.0% clear, 25.0% cloudy, and 50.0% intermediate days. Lower intermediate sky accounted for 24.0% and upper intermediate sky for 26.0%. In 2014, no acceptable days were recorded. A total of 100.0% of days were unacceptable, with 26.0% clear, 26.0% cloudy, and 48.0% intermediate days. Lower intermediate sky was 24.0% and upper intermediate sky was 26.0%.

At the Barue–1 station in 2012, 56.0% of days were acceptable, with 15.0% clear, 16.0% cloudy, and 26.0% intermediate days, including 15.0% lower intermediate sky and 11.0%

upper intermediate sky. On the other hand, 44.0% of days were unacceptable, with 11.0% clear, 11.0% cloudy, and 21.0% intermediate days, including 11.0% lower intermediate sky and 10.0% upper intermediate sky. In 2013, 56.0% of days were acceptable, with 14.0% clear, 14.0% cloudy, and 27.0% intermediate days, including 14.0% lower intermediate sky and 13.0% upper intermediate sky. Meanwhile, 44.0% of days were unacceptable, with 12.0% clear, 10.0% cloudy, and 23.0% intermediate days, including 15.0% lower intermediate sky and 11.0% upper intermediate sky. Lastly, in 2014, 58.0% of days were acceptable, with 15.0% clear, 15.0% cloudy, and 29.0% intermediate days, including 16.0% lower intermediate sky and 10.0% upper intermediate sky. On the other hand, 42.0% of days were unacceptable, with 13.0% clear, 11.0% cloudy, and 18.0% intermediate days, including 19.0% lower intermediate sky and 7.0% upper intermediate sky.

At the Barue–2 station, the breakdown of acceptable and unacceptable days varied over the years. In 2012, 56.0% of days were acceptable, with 13.0% clear, 14.0% cloudy, and 26.0% intermediate. On the other hand, 44.0% of days were unacceptable, with 12.0% clear, 11.0% cloudy, and 20.0% intermediate. Moving on to 2013, 52.0% of days were acceptable, with 13.0% clear, 15.0% cloudy, and 28.0% intermediate. Meanwhile, 48.0% of days were unacceptable, with 11.0% clear, 11.0% cloudy, and 22.0% intermediate. Finally, in 2014, 52.0% of days were acceptable, with 12.0% clear, 13.0% cloudy, and 27.0% intermediate. Conversely, 48.0% of days were unacceptable, with 12.0% clear, 13.0% cloudy, and 27.0% intermediate.

At Chipera station in 2012, out of the total 62.0% of acceptable days, 15.0% were clear days, 15.0% were cloudy days, and 31.0% were intermediate days, with 16.0% of lower intermediate sky and 14.0% of upper intermediate sky. On the other hand, of the total 38.0% of unacceptable days, 9.0% were clear days, 10. 0% were cloudy days, and 19.0% were intermediate days, with 10.0% being lower intermediate sky and 8.0% upper intermediate sky. In 2013, out of the total 52.0% of acceptable days, 12.0% were clear days, 15.0% were cloudy days, and 27.0% were intermediate days, with 15.0% lower intermediate sky and 12.0% upper intermediate sky. Conversely, of the total 48.0% of unacceptable days, 12.0% were clear days, 12.0% were cloudy days, and 24.0% were intermediate days, with 13.0% being lower intermediate sky and 11.0% upper intermediate sky.

3.2. Correlation of the Clear Sky Index Coefficient between Station Sensor Pairs

The spatial autocorrelation of the clear sky index coefficients, in relation to the distance between the pair of pyranometers d_{ij}, shows a decrease for both acceptable and unacceptable days as illustrated in Figure 12. This decrease is observed across different classes of days, including clear (Figure 12a), cloudy (Figure 12b), intermediate (Figure 12c), and all types of days when considered together. Specifically, the decrease in autocorrelation occurs as the distance between the pair of d_{ij} sensors increases along the eastern channel of Mozambique, from the Province of Maputo to Inhambane and the Province of Sofala.

It is worth noting that a global analysis also confirms this result, although there are some fluctuations. These fluctuations were also observed in the study conducted by Marcos et al. (2015) [52], which focused on the spatial-temporal evaluation of solar energy. In their study, a high number of radiometers were used, spaced closely together, and the classification of types of days was based on a variability index. Interestingly, the correlation between correlation coefficients resulted in a decorrelation pattern as the distance between the sensors increased.

Similar results were obtained by Lohlman et al. (2018) [10] in their study of an area with a large number of pyranometers. They found numerous decorrelative correlation points, further supporting the observed decrease in autocorrelation with increasing distance.

In the examination of interprovincial distances, as well as interprovincial and interregional kilometers depicted in Figure 12, it is observed that the decline in solar energy levels varies significantly across different stations. The Maputo–1 and Nhamadzi stations show a substantial decrease, while Ndindiza, Barue–1, and Barue–2 exhibit a lesser decline. On the other hand, Pembe and Chipera stations are positioned above the adjusted correlative curve, displaying high solar energy intensity with occasional deterministic fluctuations.

The decline is particularly noticeable on days deemed unacceptable, where sudden experimental GHI values are observed, which are uncommon in measurements. These findings suggest that the record-breaking decrease may be attributed to solar radiation caused by solar flares and other extraordinary solar events.

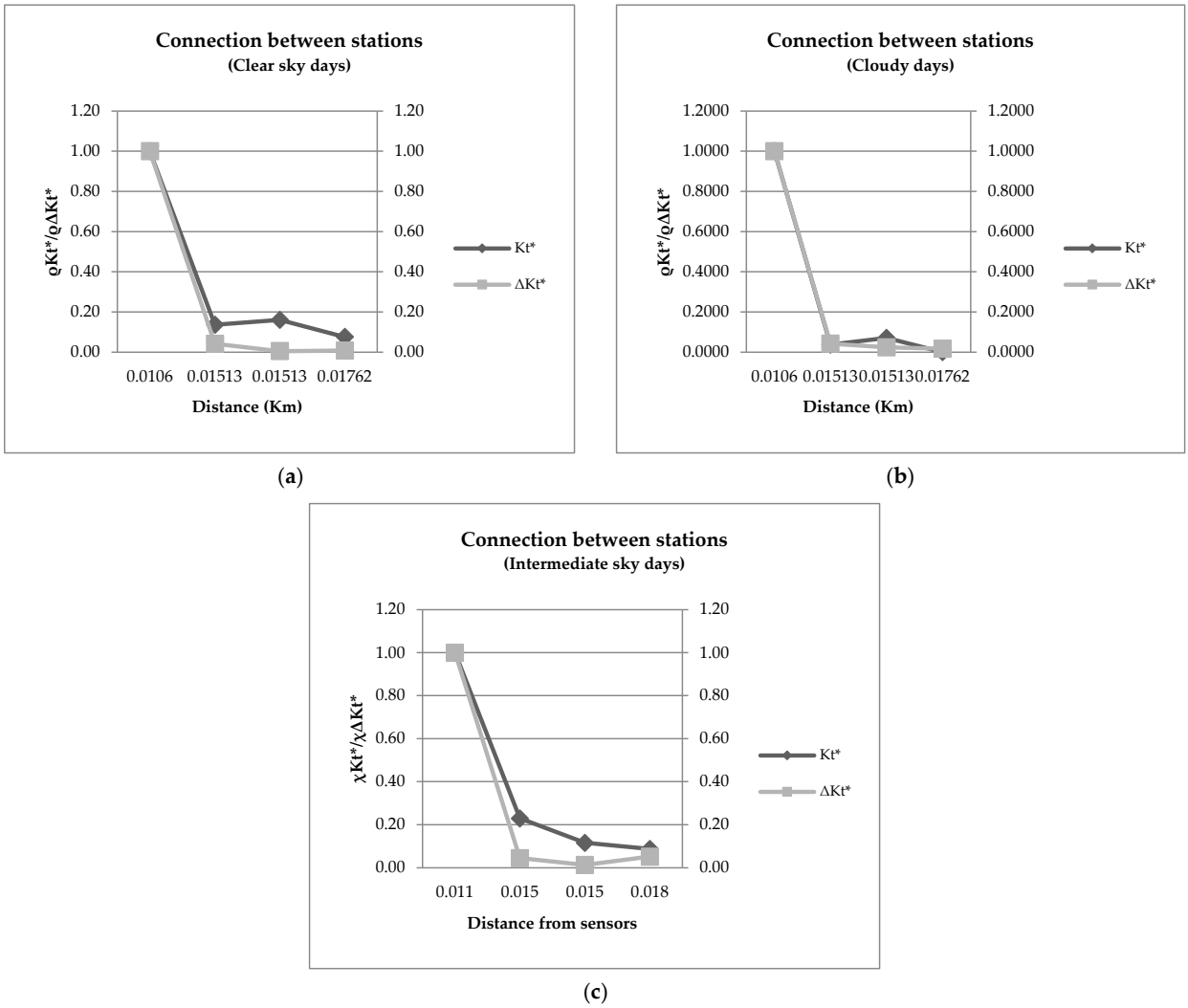

Figure 12. Systematic connection between stations throughout the southern and mid region of Mozambique for acceptable days of the following types: (**a**) Clear sky; (**b**) Cloudy sky; and (**c**) Intermediate sky.

3.3. The Temporal Assessment of the Clear Sky Index and Its Increments

Figure 13 displays the growth pattern of the clear sky index over time intervals of 1 and 10 min. Prior to this analysis, the three types of sky (clear, intermediate, and cloudy) were categorized, and the results were examined simultaneously for all three types. The probability density functions (PDFs) exhibit a concentrated peak at the center, indicating a high likelihood of increments. The PDF gradually decreases and widens on either side, forming extensive tails. This pattern aligns with previous findings by Lave and Kleissl (2010) [64] and van Haaren et al. (2014) [65], who conducted comprehensive studies using numerous pyranometers in measurement campaigns. These studies provided a clearer understanding of the subject compared to solar plants, highlighting the impact of plant capacity on increment variations. Consequently, this analysis sheds light on the probabilistic fluctuations of the clear sky index, which pose a significant challenge to solar efficiency and the overall output of solar plants.

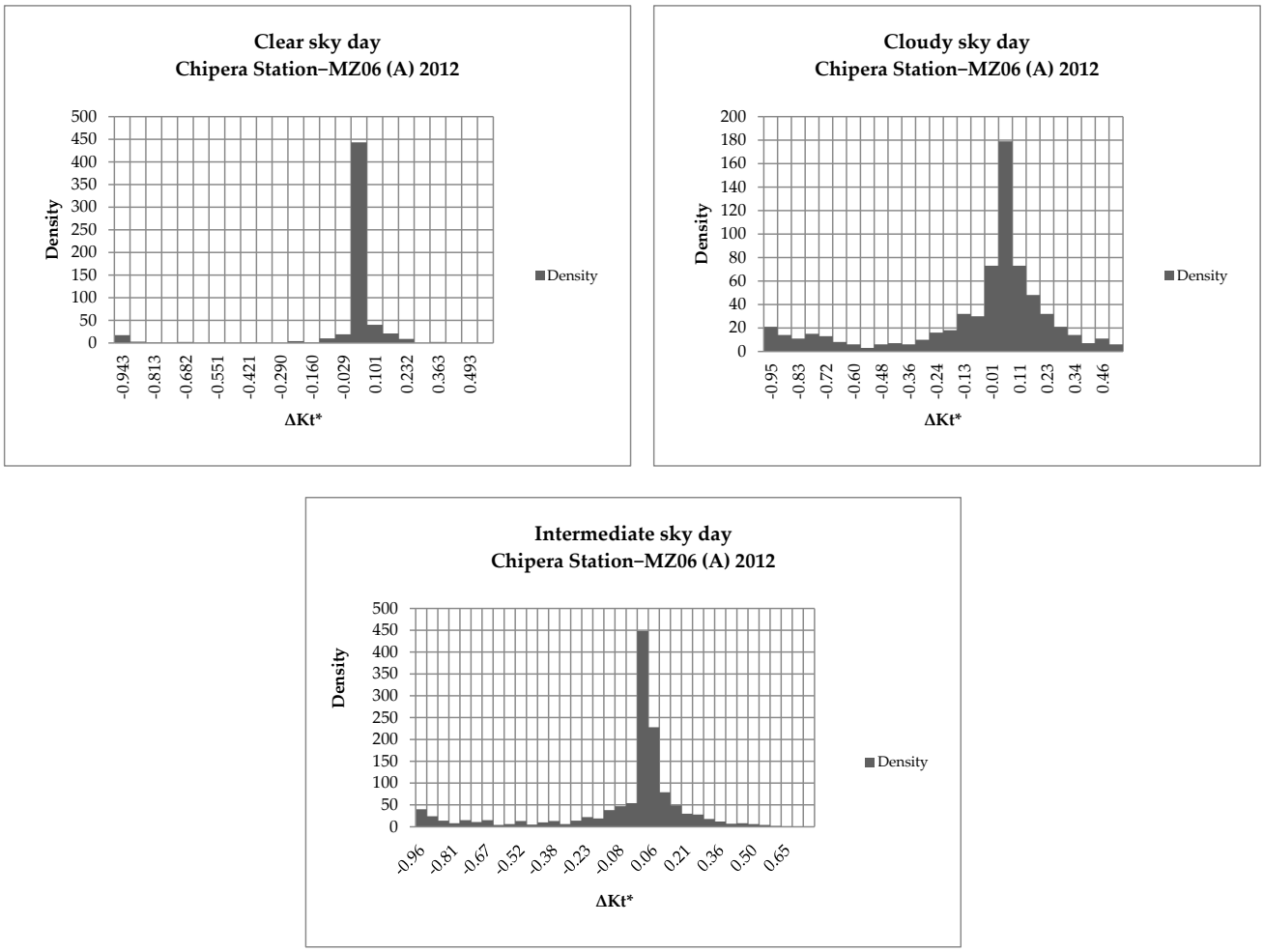

Figure 13. Distribution of ΔK_t^* variability on acceptable and unacceptable days.

The evaluation of solar energy accessibility in various stations along the eastern channel of Mozambique reveals distinct patterns depending on the weather conditions. On cloudy days, there is a prominent central peak with less pronounced tails. Similarly, clear sky days exhibit a strong central peak, but with taller, broader, and flatter tails. On days with intermediate sky conditions, the central peak is wider and the tails are much flatter. These observations indicate that there is a higher probability of experiencing significant changes in cloud cover, leading to large excursions in solar energy availability. However, the probability density graph demonstrates a gradual decrease, as the frequency of ΔK_t^* values outside the range of [–1,1] is higher. This suggests that there is a higher likelihood of transitioning from cloudy to clear and then to intermediate skies.

The frequency of values close to zero, as depicted in Figure 14, is lower on clear sky days and higher on cloudy sky days. However, they can also occur on days with intermediate sky conditions and sporadically in the assessment conditions of all three sky types. Conversely, the occurrence of values near 1 is more common in clear sky conditions, occurs occasionally in intermediate conditions, and occurs sporadically when observing all three sky types, with a reduced frequency in cloudy sky conditions.

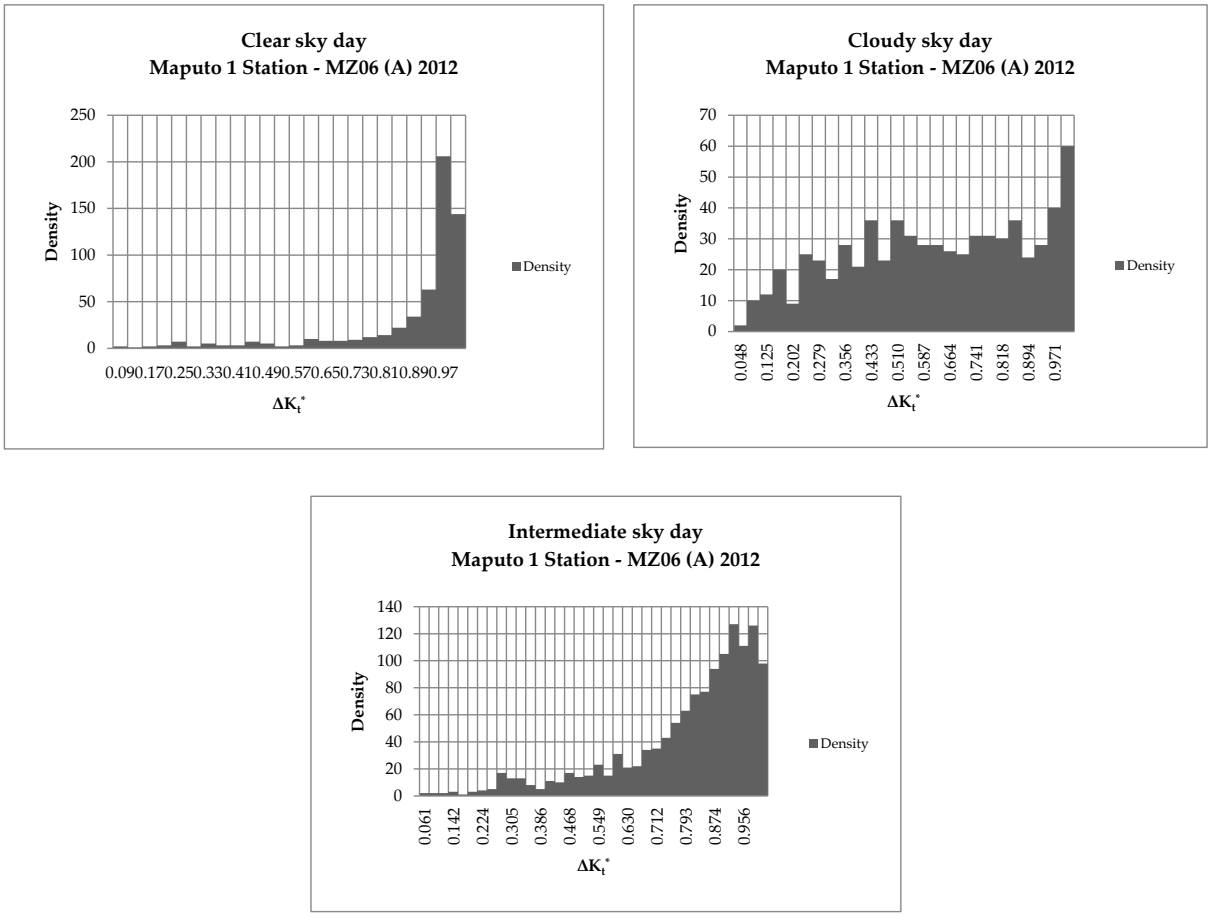

Figure 14. Distribution of K_t^* variability on clear sky days.

3.4. Correlation of Two-Point Increments Using Different Methods

To thoroughly examine the spatio-temporal and regression aspects of the entire field in the study area, we conducted an analysis on the correlation between two points using K_t^* increment coefficients. In Figure 15, we specifically focused on pairs of sensors that shared the same type of sky. For instance, Figure 15a illustrates the correlation coefficients of the clear sky index as it relates to the distance between sensor pairs at clear days.

In Figure 15, the incremental correlation structure relative to the length scale of inter-provincial study distances is demonstrated, resulting in a decorrelation of the clear sky index coefficient along the analysis path. The solar radiation sample is defined as the minimum distance from the point of origin of the measurement campaign where the correlation coefficient of the clear sky index equals 0.30, determined after evaluating solar radiation and classifying different types of classes that converge to the same coefficient mean.

The correlation distances between fixed station points generally increase with longer time intervals, transitioning from less predominant cloudy conditions to more prevalent clear skies, and then to intermediate sky conditions, which are mostly prevalent in almost all stations in the channel-east region of Mozambique (a potential issue in the utilization of solar energy).

The data in Figure 15a,b show a smooth decorrelation mechanism under varying sky conditions with K_t^* increments and short time intervals $t = 1$ min. However, Figure 15c displays a measurable decorrelation for intermediate sky types (Most models are not capable of capturing the correlation structure for intermediate sky conditions). Furthermore, when considering all sky types in each season, a decorrelation of solar energy is evident along the eastern canal section.

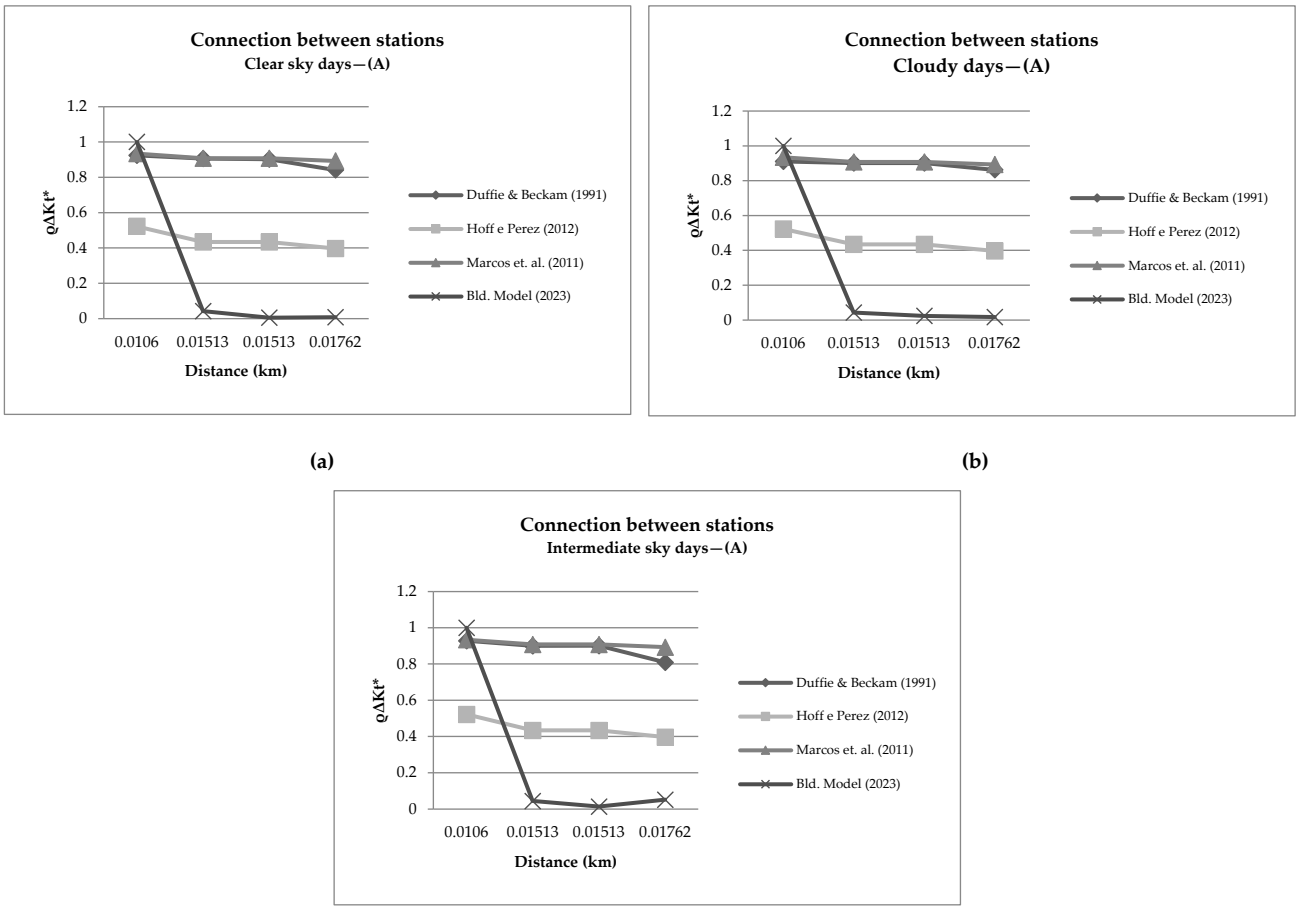

Figure 15. Spatial correlation coefficients of two stations along the southern and mid region of Mozambique for acceptable days of the following types: (**a**) Clear sky, (**b**) Cloudy sky, and (**c**) Intermediate sky [1,12,52,54].

In a separate analysis, the Maputo station exhibits a high energy content extending south of Inhambane, while in the mid region of the east−channel of Mozambique Nhamadzi shows even higher energy content running along an adjusted curve towards the Chipera station. These findings highlight the variations in energy distribution across different locations in the region, supported by correlation validation methods such as those used by Marcos et al. (2011) [52] and Hoff & Perez (2010) [13] for cloud speeds up to 6 m/s. The decorrelation patterns observed align with the model proposed by Wilson & Tanaka (2018) [54], indicating that decorrelation can be smooth on clear days and cloudy, or measurable for intermediate sky conditions. Duffie & Beckman, (1991) [1] also discovered the aspect related to solar energy decorrelation.

By increasing the decorrelation length, the correlation decay or effective decorrelation for short scale distances $d = tv\left(\rho^{-1} - 1\right)$ can be enhanced. For a correlation coefficient of approximately 0.30, this adjustment corresponds to an intermediate value of model speed. However, beyond this point, correlations diminish at a much quicker rate ranged in 0.6 and 0.8 km for velocities next to 4 and 6 m/s.

3.5. Accessibility from a Regressive and Correlative Point of View of Solar Energy

The comparison of the theoretical radiation in clear skies and the horizontal experimental global solar radiation on the earth's surface in the southern and mid region of Mozambique, based on annual observations in 2012 with consistent measurements (Figure 16), indicates that the Nhamadzi and Chipera stations have the highest potential

for full solar radiation availability, with approximately 68.0% and 67.0% of acceptable days, respectively. Following closely are the Barue–2 and Barue–1 stations, with around 57.0% and 55.0% availability.

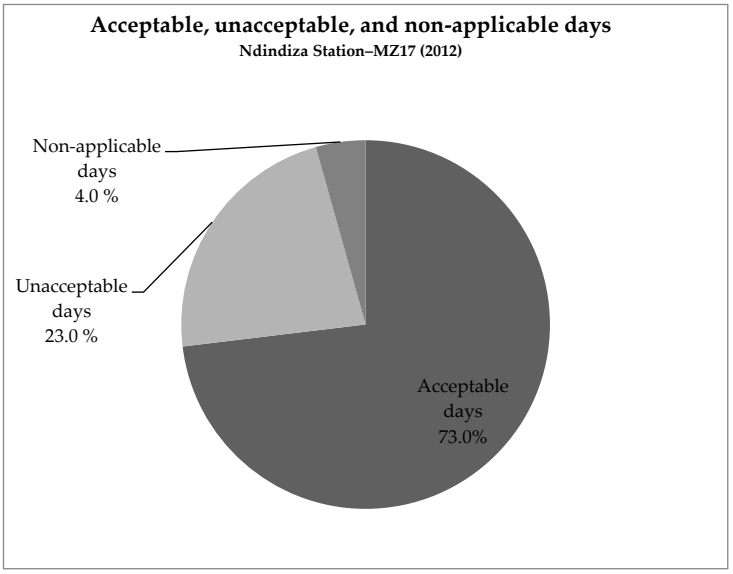

Figure 16. Quantification of acceptable, unacceptable, and non-applicable days observed during 2012 at the Ndindiza station in Gaza.

The correlative analysis revealed a decorrelation of energy in the southern region from Maputo–1 to Pembe and in the central region from Nhamadzi to Chipera. However, when considering the entire section, the decorrelation is intertwined with energy fluctuations in the central region of the channel. The standard decorrelation curve reflects the average accessibility of the stations, with Ndindiza, Massangena, Barue–1, and Barue–2 stations prevailing in the intermediate region of the decorrelation. These stations exhibit characteristics that suggest potential for utilizing solar energy and an average of over 50.0% of the estimated average incidence energy availability in the study area. Figure 16, which is applied to the Ndindiza station, serves as an example illustrating the true intensity of energy accessibility in the region through acceptable and unacceptable days. The latter are influenced by various factors such as multiple reflections of solar radiation, cloud cover, solid particles in the atmosphere, and dispersion that may affect the readings of the radiometers. Despite these challenges, they do not pose significant obstacles. Additionally, conducting a group analysis of unacceptable days, after eliminating outliers, in conjunction with acceptable days, enhances the overall feasibility of the study.

In the southern region, the evaluation of acceptable days shows that the Pembe, Ndindiza, and Massangena stations have higher levels of access to solar energy with an estimated potential of 81.0%, 73.0%, and 72.0%, respectively. The Maputo–1 station has a slightly lower estimated access of 62.0% due to incomplete sampling. When it comes to unacceptable days, Ndindiza and Massangena stations show a greater potential for the accessibility of solar energy at around 23.0% and 18.0%, while Pembe and Maputo–1 have potentials of around 20.0% and 18.0%, respectively.

Moving on to the central region, the evaluation of acceptable days reveals a lower potential for solar energy accessibility at the Barue–1 and Chipera stations, with estimates of around 68.0% and 67.0%, respectively. The average potential in Barue–2 and Chipera is around 57.0% and 55.0%. In terms of unacceptable days, Barue–1 and Barue–2 show a higher accessibility potential of around 15.0% and 26.0%, while Chipera and Nhamadzi have lower potentials of 14.0% and 26.0%, respectively.

The region's remarkable access to solar energy, particularly for electrification and other purposes, highlights the prevalence of solar energy and its impact on uneven heating. This leads to the movement of air masses from areas with higher solar energy accessibility to

those with less, in an effort to achieve equilibrium. However, the seasonal variations along the decorrelation curve, characterized by both high and sometimes moderate features, result in fluctuations in solar energy. These fluctuations are primarily caused by various atmospheric phenomena that significantly diminish the amount of solar energy reaching the Earth's surface. This ultimately affects the overall enjoyment of solar energy.

3.6. Variability in the Standardized Deviation of the Clear Sky Index and Its Increment

The availability of solar energy in the east−channel region of Mozambique is determined to be the most prevalent, with over 50.0% of the total power estimated in each station. The standardized assessment of the variability in average area quantities in relation to the relative standard deviation indicates that the reduction in variability is more rapid for shorter increments of time compared to longer ones. This trend is illustrated in Figure 17. However, the decrease in variability is slower for cloudy conditions than for other types of skies.

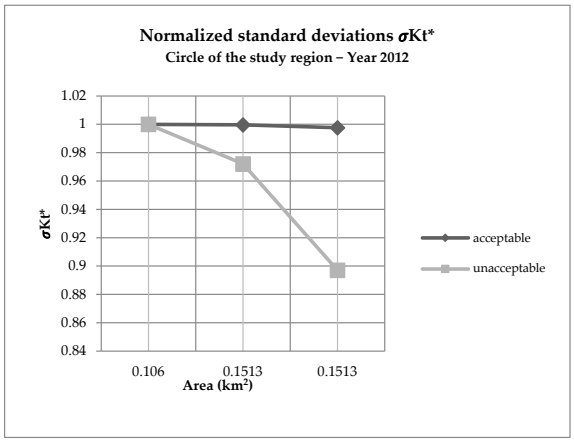

(**a**)

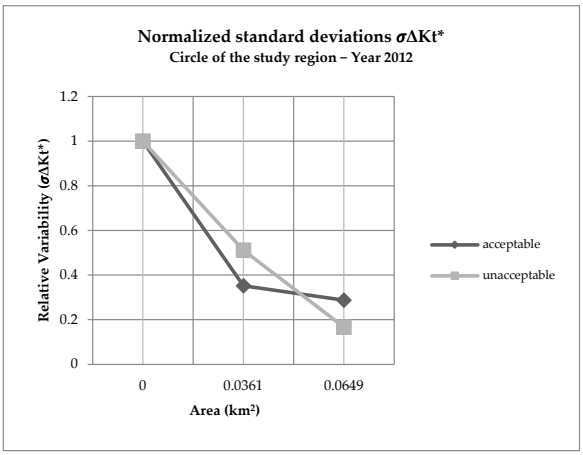

(**b**)

Figure 17. The normalized standard deviations for the area's increments, in both the acceptable and unacceptable days, are observed for two factors: (**a**) the clear sky index and (**b**) the clear sky index increments.

This study examines the daily deviation patterns each year in relation to different categories of days susceptible to deterministic fluctuations. In Figure 17a, it is evident that days deemed acceptable exhibit a strong correlation and high values of normalized deviation and the clear sky index, along with an increase in accuracy in their quantification. Conversely, unacceptable days display a noticeable correlation, with significantly lower values of normalized deviation and the clear sky index, as well as a smaller increase, indicating lower precision in their dispersion due to various factors.

However, Figure 17b demonstrates that there is a gradual decrease in the relative variability of acceptable days for both the normalized deviation of the K_t^* and its increment. This decline becomes noticeable as the K_t^* deviates towards less than 0.3. Furthermore, the analysis of unacceptable days reveals an irregular decrease, but still within the same order of clear sky indices. This irregularity is due to the range of values represented by this lineage.

Nevertheless, in the southern and mid regions of Mozambique, the energy decorrelation tends to follow a normalized deviation pattern that aligns with the energy decorrelation along the eastern-channel, as observed in the selected stations. This indicates above-average accessibility to solar energy with a regular distribution. However, it is crucial to accurately quantify the extreme fluctuations in solar irradiance in order to address various issues that may arise in the operation of a solar plant.

3.7. Regression of the Clear Sky Index and Its Increments

In the mid region of Mozambique, there is a significant occurrence of high PV power.

The analysis of solar energy regression in the eastern−channel of Mozambique examines the relationship between solar energy in that particular region. In Figure 18, the regression is presented for days with acceptable solar energy levels, whereas Figure 19 displays the deviation from the regression for unacceptable days. This deviation is measured in terms of clear sky index regression coefficients.

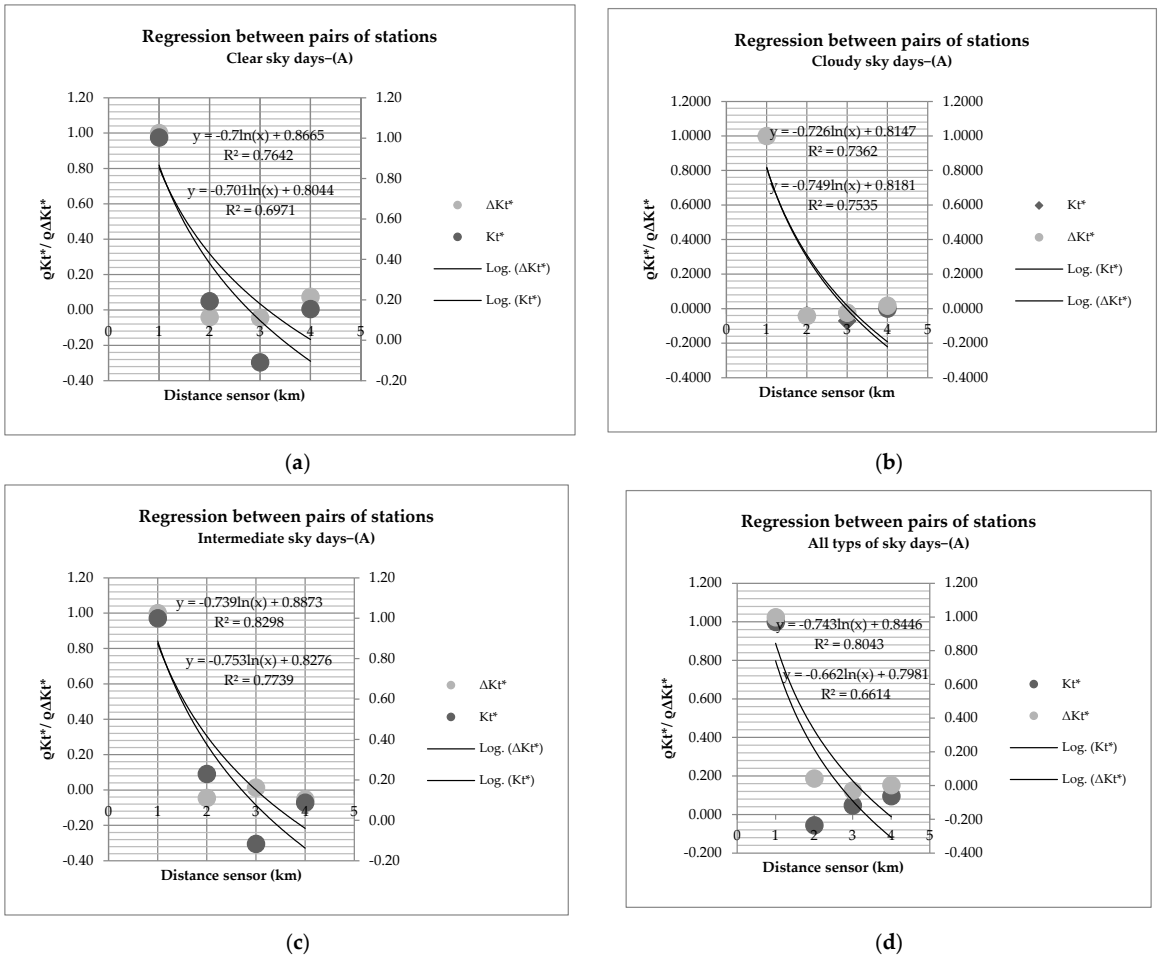

(**a**) (**b**)

(**c**) (**d**)

Figure 18. Illustrates the regression analysis conducted on pairs of states within the eastern canal region of Mozambique, specifically focusing on acceptable days, in the conditions of: (**a**) clear sky days, (**b**) cloudy sky days, (**c**) intermediate sky days and (**d**) all sky days.

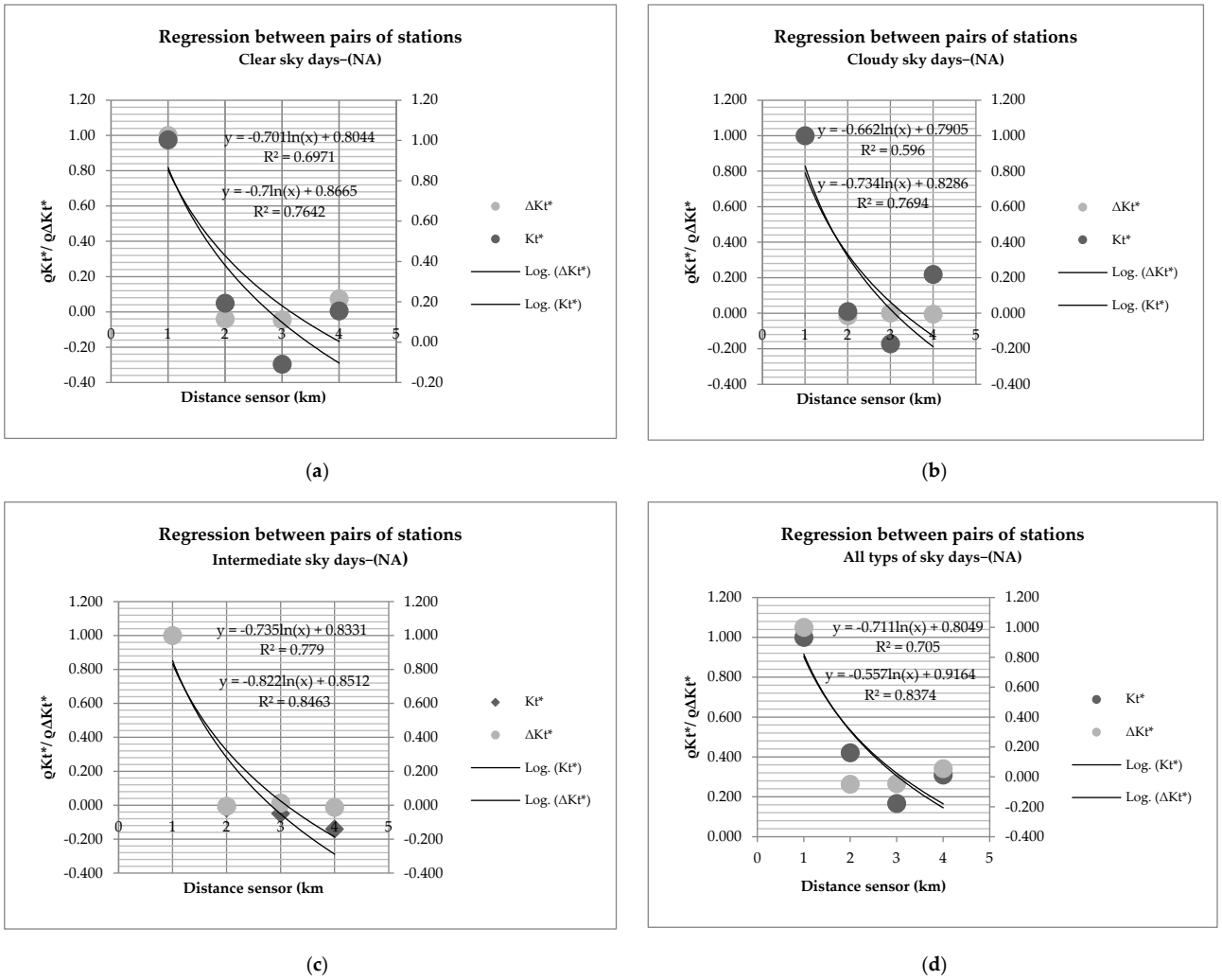

Figure 19. Regression analysis performed on pairs of stations within the channel-east region of Mozambique, but this time focusing on unacceptable days, in the conditions of: (**a**) clear sky days, (**b**) cloudy sky days, (**c**) intermediate sky days and (**d**) all sky days.

The regression coefficients for the clear sky index and their increase for acceptable days are, R^2 = 0.8 and 0.88 for clear days as depicted in Figure 18a, R^2 = 0.7 and 0.8 for cloudy days as depicted in Figure 18b, R^2 = 0.7 and 0.8 for intermediate sky days as depicted in Figure 18c, and R^2 = 0.7 and 0.7 for all sky types as depicted in Figure 18d. For unacceptable days, the regression coefficients for, for clear days R^2 = 0.7 and 0.7 as depicted in Figure 19a, for cloudy days R^2 = 0.6 and 0.8 as depicted in Figure 19b, intermediate sky days are R^2 = 0.7 and 0.8 as depicted in Figure 19c, and for all sky types R^2 = 0.7 and 0.8 as depicted in Figure 19d.

The trajectory back to the norm is more noticeable on days with intermediate sky conditions, as illustrated in Figures 18c and 19c, in comparison to other types of sky conditions.

The region shows a non-linear regression with a tendency towards logarithmic behavior, with a regression coefficient of approximately 0.8 and 0.8 for all types of days. The regression analysis indicates that the deviation pattern from the normalized curve is more pronounced on non-acceptable days compared to acceptable days. The regressively accessible solar energy maintains consistency in relation to correlative access solar energy, as the linear regression coefficient matrices are standardized and adjusted to logarithmic models to ensure uniformity in accounting for accessibility on acceptable days.

4. Discussion

In the south and mid region of Mozambique, there is a significant occurrence of high PV power under clear and intermediate sky conditions. This is marked by a consistent increase in the maximum power point (MPP), which poses a threat to the reliability of the network. In cloudy conditions, PV plants may require hybridization to mitigate the temporary lack of PV generation, especially when facing high, intermediate, and low PV fluctuations. Studies conducted by Mucomole et al. (2023) [2] and Zhu et al. (2019) [66] focus on sizing PV systems for autonomous operations by considering days with the highest radiation as a key factor for generation (clear days with high radiation and cloudy days with less radiation). This approach helps in determining the appropriate site size based on daily energy generation, which can then be injected into the grid. On the contrary, research by Marcos et al., (2011) [52], Hoff & Perez, (2010) [13], and (Lohmann, 2016) [10] suggests that clear and intermediate conditions may have adverse effects on the electrical grid. These studies also quantify the variability of days throughout the year, highlighting potential patterns such as a hot and rainy season with clear and intermediate days, as well as a cold and dry season with predominantly cloudy days. Understanding these factors is crucial for accurately projecting the reliability of PV systems across the region.

The distribution of acceptable days (Figures 8 and 9) exhibits a consistent pattern compared to unacceptable days (Figures 10 and 11), which are attributed to measurement errors or external factors like cloud reflections, solar radiation absorption in the atmosphere, and other interferences observed at the monitoring sites.

The relationship between correlation coefficients and distance is illustrated in Figures 12 and 15. These coefficients tend to be higher at the starting point in Maputo–1 and Nhamadzi and lower on the arrival route in Pembe and Chipera. Similar findings have been observed in the research conducted by Perez et al. (2012) [53], which focused on decorrelation distances below 10 km and temporal lags below 15 min using virtual pyranometer networks. The temporal resolutions of single-point measurements in their study were as low as 20 s. Additionally, Lohmann, (2018) [49] found that decorrelation distances for linear distance scale and time intervals may not be applicable to observed multipoint samples of K_t^* fields at very high spatiotemporal resolutions. Hoff & Perez, 2012 [12] also support this relationship by presenting a linear scale of decorrelation distances based on satellite-derived data in Figures 12 and 15.

When comparing intermediate sky days to cloudy and clear skies, it is observed that intermediate sky days have flatter arms and a higher probability density of strong fluctuations, as shown in Figure 13. However, Lohmann, (2016) [49] reports that strong fluctuations can be even greater when considering inclined photovoltaic panels.

The Barue–1 and Barue–2 stations exhibit a potentially higher intermediate energy power between the Chipera stations compared to Nhamadzi. This difference is attributed to heat flow transport phenomena, where the mass flow of solar energy follows the seasonal direction to establish the solar energy balance.

The results of the regression analysis indicate that the deviation pattern from the normalized curve is more pronounced on days that are considered non-acceptable compared to acceptable days. The accessibility of solar energy, when analyzed regressively, remains consistent when compared to the accessibility based on correlation. This is achieved by adjusting the standardized linear regression coefficient matrices to logarithmic models, ensuring uniformity in accounting for accessibility on acceptable days. In a study conducted by Lam & Li (1996) [58], and Ibrahim et al., (2012) [42] a similar methodology was employed to investigate the relationship between global radiation and regression. The findings of this study were highly promising, as they successfully estimated the Global Horizontal Irradiance (GHI) in a specific area. Similarly, the current study also quantifies the regression process of solar energy accessibility by inversely correlating a pair of stations.

5. Conclusions

The electrification of rural areas is being combined with the utilization of clean energy sources like solar PV energy, which is efficient, clean, and stable. This trend is growing worldwide, particularly in the south and mid-western region of Mozambique where there is a lack of access to electricity. However, the implementation of PV systems in this region has faced challenges, resulting in a short lifespan. These challenges are caused by various factors that affect the functioning of the systems, including the fluctuation of solar energy and other important factors that impact the planning and reliability of future PV electrical networks and other solar energy projects. By analyzing data collected during the FUNAE campaign in Maputo–1, Ndindiza, Massangena, Pembe, Nhamadzi, Barue (Barue–1 and Barue–2), and Chipera, the accessibility of and variability in solar energy in the south and mid-west region of Mozambique were determined on a short-term scale. From this analysis, the following can be concluded:

The solar energy potential in the south and mid-west region is significant. In 2012, at the Maputo–1 and Chipera station, approximately 24.74% of the days were clear, 49.48% were intermediate, and 25.77% were cloudy. Moving on to 2013, the percentages were estimated as 24.14% clear days, 50.86% intermediate days, and 27.99% cloudy days. At the Pembe and Nhamadzi station, in 2012, an estimated 25.0% of the days were clear, 48.53% were intermediate, and 27.94% were cloudy. In 2013, the percentages were 25.0% clear days, 50.0% intermediate days, and 25.0% cloudy days. In 2014, the estimates were 26.0% clear days, 48.0% intermediate days, and 26.0% cloudy days. At the Ndindiza and Barue–1 station, in 2012, the estimated percentages were 25.93% clear days, 47.22% intermediate days, and 26.85% cloudy days. In 2013, the estimates were 26.04% clear days, 50.23% intermediate days, and 24.19% cloudy days. Finally, in 2014, the estimates were 28.45% clear days, 47.51% intermediate days, and 25.96% cloudy days. At the Massangena and Barue–2 station, in 2012, approximately 23.48% of the days were clear, 46.09% were intermediate, and 24.78% were cloudy. In 2013, the estimates were 24.07% clear days, 50.0% intermediate days, and 25.93% cloudy days. Lastly, in 2014, the estimates were 24.45% clear days, 67.28% intermediate days, and 26.20% cloudy days.

The frequency density of values near zero is lower compared to values near 1 on clear sky days, but this relationship is reversed on cloudy days. On days with intermediate sky conditions, the frequency density of observations for values near 1 is lower than those near 0.66, and values below 0.02 are observed for K_t^* values near 0. The analysis of all sky types shows that K_t^* exhibits similar characteristics to other days, and these values fall within the theoretical radiation spectrum, ranging from -1 to 1.

When the distances between pairs of pyranometers d_{ij} exceed 10^3 km, the solar energy decrease along the correlative curve is significant in Nhamadzi, and reduced in Barue–1 and Barue–2. However, above the adjusted correlative curve lies the Chipera station.

By calculating the average of the sensor K_t^* increments, one can obtain an approximation of the output variability in a collection of PV installations situated in different locations. Nevertheless, it is worth noting that the intermediate sky days pose a greater challenge in terms of PV power fluctuations and exhibit higher absolute values of ΔK_t^*.

Intermediate sky daytime conditions with significant decay in the K_t^* arms have demonstrated sub-minute incremental PDFs with more uniform tails and increased likelihood of intense fluctuations compared to overcast and clear skies.

Correlation coefficients typically decline as distance increases and rise with fluctuation timescales.

The assessment of the Maputo–1 and Chipera stations in 2013, as well as the Nhamadzi station in 2013 and 2014, faced obstacles due to various factors such as cloud interference and the obstruction of solar energy measurement. However, the Ndindiza and Barue–1 stations exhibit a greater potential for solar energy compared to the Massangena and Barue–2 stations. In 2013, the Ndindiza and Barue–1 station recorded approximately 71 and 65.0% more solar energy, respectively. Similarly, in 2014, the difference was around 75% and 70.0% more. This disparity was also observed in both 2013 and 2014, with the Ndindiza and Barue–1 station

having 63.0% and 64.0% more solar energy, respectively. This variation can be attributed to the phenomenon of heat flow transport, where solar energy moves in a seasonal direction to establish equilibrium.

The area exhibits a non-linear regression pattern that leans towards logarithmic behavior. The regression coefficient for clear sky and its increment is approximately 0.8 and 0.87, respectively, for all types of days.

6. Patents

This research article appears as one of the first obligations in obtaining a Doctorate degree in the Doctoral Course in Energy Science and Technology, at Eduardo Mondlane University, which the main author is attending.

Author Contributions: In this research article, the conceptualization, methodology, validation, and formal analysis, were performed by F.V.M.; the investigation, resources, data curation, writing, preparation of the original draft, writing, review and editing, acquisition of funding, and visualization and software were performed by the main authors F.V.M. and L.L.M.; the supervision and project administration were performed by F.V.M. and C.A.S.S.; and the advanced curation of data and writing and supervision were performed by F.V.M., C.A.S.S. and L.L.M. All authors have read and agreed to the published version of the manuscript.

Funding: This research is funded by CS-OGET, of the Faculty of Engineering of Eduardo Mondlane University within the scope of doctoral research.

Data Availability Statement: The data that back up the reported outcomes are accessible on the NOAA website at https://www.noaa.gov/weather [27] and the NASA POWER website at https://power.larc.nasa.gov/data-access-viewer/ [28], Accessed 10 December 2023. Additional data that support the conclusions of this research have not been released and can be obtained from INAM [51], FUNAE [56], UEM, or upon request by contacting the corresponding author.

Acknowledgments: We express our gratitude to the FUNAE [56], entities for their assistance in providing us with sample data from the campaign conducted between 2012 and 2014. We would also like to thank INAM [51] for supplying us with the sample of solar radiation data spanning from 1995 to 2023, and for granting us access to their facilities for training and experimental tests. Additionally, we extend our appreciation to the Department of Physics at Eduardo Mondlane University for generously making their facilities available for real-time testing and measurements of the latest solar energy behavior. Their provision of a laboratory for data processing greatly contributed to the compilation of this research. Lastly, we would like to acknowledge CS-OGET for their support, as it played an integral role in the culmination stage of this doctoral research.

Conflicts of Interest: The authors declare no conflict of interest.

References

1. Duffie, J.A.; Beckman, W.A. *Solar Engineering of Thermal Processes*; John Wiley & Sons: Hoboken, NJ, USA, 2013.
2. Mucomole, F.V.; Silva, C.A.S.; Magaia, L.L. Temporal Variability of Solar Energy Availability in the Conditions of the Southern Region of Mozambique. *Am. J. Energy Nat. Resour.* **2023**, *2*, 27–50. [CrossRef]
3. Kreuwel, F.P.M.; Knap, W.H.; Visser, L.R.; Van Sark, W.G.J.H.M.; Vilà-Guerau De Arellano, J.; Van Heerwaarden, C.C. Analysis of high frequency photovoltaic solar energy fluctuations. *Sol. Energy* **2020**, *206*, 381–389. [CrossRef]
4. Williamson, S.; Businger, S.; Matthews, D. Development of a solar irradiance dataset for Oahu, Hawai'i. *Renew. Energy* **2018**, *128*, 432–443. [CrossRef]
5. Wenham, S.R.; Green, M.A.; Watt, M.E.; Corkish, R.; Sproul, A. (Eds.) *Applied Photovoltaics*, 3rd ed.; Routledge: London, UK, 2011; ISBN 978-1-84977-698-1.
6. IEA; IRENA; UNSD; World Bank; WHO. Tracking SDG 7: The Energy Progress Report. World Bank, Washington DC. © World Bank. 2023. Available online: https://cdn.who.int/media/docs/default-source/air-pollution-documents/air-quality-and-health/sdg7-report2023-full-report_web.pdf?sfvrsn=669e8626_3&download=true (accessed on 16 December 2023).
7. Energypedia, Energy Access Situation in Mozambique. 2023. Available online: https://energypedia.info/wiki/Situa%C3%A7%C3%A3o_de_Acesso_%C3%A0_Energia_em_Mo%C3%A7ambique (accessed on 15 December 2023).
8. Fernández, M.E.; Gentili, J.O.; Casado, A.L.; Campo, A.M. Global horizontal irradiation: Spatio-temporal variability on a regional scale in the south of the Pampeana region (Argentina). *AUC Geogr.* **2021**, *56*, 220–233. [CrossRef]
9. Karapantsios, T.D.; Hatzimoisiadis, K.A.; Balouktsis, A.I. Estimation of total atmospheric pollution using global radiation data: Introduction of a novel clear day selection methodology. *Renew. Energy* **1999**, *17*, 169–181. [CrossRef]

10. Lohmann, G.M. Solar Irradiance Variability on Small Spatial and Temporal Scales. Ph.D. Thesis, Carl von Ossietzky Universität Oldenburg, Oldenburg, Germany, 2017.
11. Aziz, T.; Ketjoy, N. PV Penetration Limits in Low Voltage Networks and Voltage Variations. *IEEE Access* **2017**, *5*, 16784–16792. [CrossRef]
12. Hoff, T.E.; Perez, R. PV Power Output Variability: Calculation of Correlation Coefficients Using Satellite Insolation Data. 2010. Available online: https://www.semanticscholar.org/paper/PV-Power-Output-Variability:-Correlation/c32816c677f3021ae2cdd41ddd745414f6c87071 (accessed on 13 January 2023).
13. Hoff, T.E.; Perez, R. Quantifying PV power Output Variability. *Sol. Energy* **2010**, *84*, 1782–1793. [CrossRef]
14. Law, E.W.; Prasad, A.A.; Kay, M.; Taylor, R.A. Direct normal irradiance forecasting and its application to concentrated solar thermal output forecasting—A review. *Sol. Energy* **2014**, *108*, 287–307. [CrossRef]
15. Lohmann, G.M.; Monahan, A.H. Effects of temporal averaging on short-term irradiance variability under mixed sky conditions. *Atmos. Meas. Tech.* **2018**, *11*, 3131–3144. [CrossRef]
16. Iqbal, M. *An Introduction to Solar Radiation*; Academic Press: Toronto, ON, Canada; New York, NY, USA, 1983; ISBN 978-0-12-373750-2.
17. Ibanez, M.; Beckman, W.A.; Klein, S.A. Frequency Distributions for Hourly and Daily Clearness Indices. *J. Sol. Energy Eng.* **2002**, *124*, 28–33. [CrossRef]
18. Luoma, J.; Kleissl, J.; Murray, K. Optimal inverter sizing considering cloud enhancement. *Sol. Energy* **2011**, *86*, 421–429. [CrossRef]
19. Trindade, A.; Cordeiro, L.C. Synthesis of Solar Photovoltaic Systems: Optimal Sizing Comparison. In *Software Verification*; Christakis, M., Polikarpova, N., Duggirala, P.S., Schrammel, P., Eds.; Lecture Notes in Computer Science; Springer International Publishing: Cham, Switzerland, 2020; Volume 12549, pp. 87–105. ISBN 978-3-030-63617-3.
20. Takilalte, A.; Harrouni, S.; Yaiche, M.R.; Mora-López, L. New approach to estimate 5-min global solar irradiation data on tilted planes from horizontal measurement. *Renew. Energy* **2020**, *145*, 2477–2488. [CrossRef]
21. Sengupta, E.M.; Habte, A.; Gueymard, C.; Wilbert, S.; Renne, D.; Stoffel, T. Best Practices Handbook for the Collection and Use of Solar Resource Data for Solar Energy Applications: Second Edition. *Renew. Energy* **2017**, *2*, 257–265.
22. Yordanov, I.; Velikova, V.; Tsonev, T. Plant Responses to Drought, Acclimation, and Stress Tolerance. *Photosynthetica* **2012**, *38*, 171–186. [CrossRef]
23. Jerez, S.; Tobin, I.; Turco, M.; Jiménez-Guerrero, P.; Vautard, R.; Montávez, J.P. Future changes, or lack thereof, in the temporal variability of the combined wind-plus-solar power production in Europe. *Renew. Energy* **2019**, *139*, 251–260. [CrossRef]
24. Jerez, S.; Trigo, R.M.; Sarsa, A.; Lorente-Plazas, R.; Pozo-Vázquez, D.; Montávez, J.P. Spatio-temporal Complementarity between Solar and Wind Power in the Iberian Peninsula. *Energy Procedia* **2013**, *40*, 48–57. [CrossRef]
25. Hassan, M.A.; Bailek, N.; Bouchouicha, K.; Ibrahim, A.; Jamil, B.; Kuriqi, A.; Nwokolo, S.C.; El-kenawy, E.-S.M. Evaluation of energy extraction of PV systems affected by environmental factors under real outdoor conditions. *Theor. Appl. Climatol.* **2022**, *150*, 715–729. [CrossRef]
26. Koudouris, G.; Dimitriadis, P.; Iliopoulou, T.; Mamassis, N.; Koutsoyiannis, D. A stochastic model for the hourly solar radiation process for application in renewable resources management. *Adv. Geosci.* **2018**, *45*, 139–145. [CrossRef]
27. NOAA. NOAA's National Weather Service Is Building a Weather-Ready Nation by Providing Better Information for Better Decisions to Save Lives and Livelihoods. Available online: https://www.noaa.gov/weather (accessed on 10 December 2023).
28. NASA. Power data access viewer: Prediction Of Worldwide Energy Resource. Available online: https://power.larc.nasa.gov/data-access-viewer/ (accessed on 10 December 2023).
29. Behr, H.; Jung, C.; Trentmann, J.; Schindler, D. Using satellite data for assessing spatiotemporal variability and complementarity of solar resources—A case study from Germany. *Meteorol. Z.* **2021**, *30*, 515–532. [CrossRef]
30. Kühnert, J.; Lorenz, E.; Heinemann, D. Satellite-Based Irradiance and Power Forecasting for the German Energy Market. In *Solar Energy Forecasting and Resource Assessment*; Elsevier: Amsterdam, The Netherlands, 2013; pp. 267–297. ISBN 978-0-12-397177-7.
31. Amillo, A.G.; Ntsangwane, L.; Huld, T.; Trentmann, J. Comparison of satellite-retrieved high-resolution solar radiation datasets for South Africa. *J. Energy S. Afr.* **2018**, *29*, 63–76. [CrossRef]
32. Kumar, D.S.; Maharjan, S.; Albert; Srinivasan, D. Ramp-rate limiting strategies to alleviate the impact of PV power ramping on voltage fluctuations using energy storage systems. *Sol. Energy* **2022**, *234*, 377–386. [CrossRef]
33. Lorenzo, A.T. *Short-Term Irradiance Forecasting Using an Irradiance Monitoring Network, Satellite Imagery, and Data Assimilation*; The University of Arizona: Tucson, AZ, USA, 2017.
34. Moerkerken, A.; Duijndam, S.; Blasch, J.; van Beukering, P.; van Well, E. Which farmers adopt solar energy? A regression analysis to explain adoption decisions over time. *Renew. Energy Focus* **2023**, *45*, 169–178. [CrossRef]
35. Morganti, M.; Salvati, A.; Coch, H.; Cecere, C. Urban morphology indicators for solar energy analysis. *Energy Procedia* **2017**, *134*, 807–814. [CrossRef]
36. Gopinathan, K.K. A simple method for predicting global solar radiation on a horizontal surface. *Sol. Wind Technol.* **1988**, *5*, 581–583. [CrossRef]
37. El-Sebaii, A.A.; Trabea, A.A. Estimation of horizontal diffuse solar radiation in Egypt. *Energy Convers. Manag.* **2003**, *44*, 2471–2482. [CrossRef]
38. Abuella, M.; Chowdhury, B. Solar power probabilistic forecasting by using multiple linear regression analysis. In Proceedings of the SoutheastCon 2015, Fort Lauderdale, FL, USA, 9–12 April 2015; pp. 1–5. [CrossRef]

39. Stević, I.; Mirjanić, D.; Stević, S. Possibilities for wider investment in solar energy implementation. *Energy* **2019**, *180*, 495–510. [CrossRef]
40. Abdul-Wahab, S.A.; Bakheit, C.S.; Al-Alawi, S.M. Principal component and multiple regression analysis in modelling of ground-level ozone and factors affecting its concentrations. *Environ. Model. Softw.* **2005**, *20*, 1263–1271. [CrossRef]
41. Dyson, M.E.H.; Borgeson, S.D.; Tabone, M.D.; Callaway, D.S. Using smart meter data to estimate demand response potential, with application to solar energy integration. *Energy Policy* **2014**, *73*, 607–619. [CrossRef]
42. Ibrahim, S.; Daut, I.; Irwan, Y.M.; Irwanto, M.; Gomesh, N.; Farhana, Z. Linear Regression Model in Estimating Solar Radiation in Perlis. *Energy Procedia* **2012**, *18*, 1402–1412. [CrossRef]
43. Arumugham, D.R.; Rajendran, P. Modelling global solar irradiance for any location on earth through regression analysis using high-resolution data. *Renew. Energy* **2021**, *180*, 1114–1123. [CrossRef]
44. Midilli, A.; Kucuk, H. Mathematical modeling of thin layer drying of pistachio by using solar energy. *Energy Convers. Manag.* **2003**, *44*, 1111–1122. [CrossRef]
45. Benghanem, M.; Joraid, A.A. A multiple correlation between different solar parameters in Medina, Saudi Arabia. *Renew. Energy* **2007**, *32*, 2424–2435. [CrossRef]
46. Brabec, M.; Paulescu, M.; Badescu, V. Statistical properties of clear and dark duration lengths. *Sol. Energy* **2017**, *153*, 508–518. [CrossRef]
47. Lohmann, G.M.; Monahan, A.H.; Heinemann, D. Local short-term variability in solar irradiance. *Atmos. Chem. Phys.* **2016**, *16*, 6365–6379. [CrossRef]
48. Gueymard, C.A. Variability in Direct Irradiance around the Sahara: Are the Modeled Datasets of Bankable Quality? In Proceedings of the SolarPACES Conference, Perpignan, France, 21–24 September 2010.
49. Lohmann, G. Irradiance Variability Quantification and Small-Scale Averaging in Space and Time: A Short Review. *Atmosphere* **2018**, *9*, 264. [CrossRef]
50. Perez, R.; David, M.; Hoff, T.E.; Jamaly, M.; Kivalov, S.; Kleissl, J.; Lauret, P.; Perez, M. Spatial and Temporal Variability of Solar Energy. *Found. Trends®Renew. Energy* **2016**, *1*, 1–44. [CrossRef]
51. INAM. Mozambique's National Institute of Meteorology, Weather and Solar Data. Available online: https://www.inam.gov.mz/index.php/pt/produtos-e-servicos/previsao-de-tempo (accessed on 10 May 2022).
52. Marcos, J.; Marroyo, L.; Lorenzo, E.; Alvira, D.; Izco, E. Power output fluctuations in large scale pv plants: One year observations with one second resolution and a derived analytic model: Power Output Fluctuations in Large Scale PV plants. *Prog. Photovolt. Res. Appl.* **2011**, *19*, 218–227. [CrossRef]
53. Perez, R.; Kivalov, S.; Schlemmer, J.; Hemker, K.; Hoff, T.E. Short-term irradiance variability: Preliminary estimation of station pair correlation as a function of distance. *Sol. Energy* **2012**, *86*, 2170–2176. [CrossRef]
54. Wilson, P.; Tanaka, O.K. Statistics, Basic Concepts —Wilson Pereira/Oswaldo K. Tanaka. 2018. Available online: https://www.estantevirtual.com.br/livros/wilson-pereira-oswaldo-k-tanaka/estatistica-conceitos-basicos/189548989 (accessed on 6 February 2023).
55. Amjad, D.; Mirza, S.; Raza, D.; Sarwar, F.; Kausar, S. A Statistical Modeling for spatial-temporal variability analysis of solar energy with respect to the climate in the Punjab Region. *Bahria Univ. Res. J. Earth Sci.* **2023**, *7*, 10.
56. FUNAE. National Energy Fund of Mozambique, Data on the solar radiation component extracted from the energy atlas. Available online: https://funae.co.mz/ (accessed on 10 May 2022).
57. Barry, J.; Munzke, N.; Thomas, J. Power fluctuations in solar-storage clusters: Spatial correlation and battery response times. *Energy Procedia* **2017**, *135*, 379–390. [CrossRef]
58. Lam, J.C.; Li, D.H.W. Regression Analysis of Solar Radiation and Sunshine Duration. *Archit. Sci. Rev.* **1996**, *39*, 15–23. [CrossRef]
59. Armstrong, S.; Hurley, W.G. A new methodology to optimise solar energy extraction under cloudy conditions. *Renew. Energy* **2010**, *35*, 780–787. [CrossRef]
60. Sarralde, J.J.; Quinn, D.J.; Wiesmann, D.; Steemers, K. Solar energy and urban morphology: Scenarios for increasing the renewable energy potential of neighbourhoods in London. *Renew. Energy* **2015**, *73*, 10–17. [CrossRef]
61. Sharif, A.; Meo, M.S.; Chowdhury, M.A.F.; Sohag, K. Role of solar energy in reducing ecological footprints: An empirical analysis. *J. Clean. Prod.* **2021**, *292*, 126028. [CrossRef]
62. Kayima, P.; Semakula, H.M.; Wasswa, H.; Mugagga, F.; Mukwaya, P.I. Analysis of the socio-economic benefits of on-grid hybrid solar energy system on Bugala island in Uganda. *Energy Sustain. Dev.* **2023**, *77*, 101332. [CrossRef]
63. Herche, W. Solar energy strategies in the U.S. utility market. *Renew. Sustain. Energy Rev.* **2017**, *77*, 590–595. [CrossRef]
64. Lave, M.; Kleissl, J.; Arias-Castro, E. High-frequency irradiance fluctuations and geographic smoothing. *Sol. Energy* **2012**, *86*, 2190–2199. [CrossRef]
65. Van Haaren, R.; Morjaria, M.; Fthenakis, V. Empirical assessment of short-term variability from utility-scale solar PV plants: Assessment of variability from utility-scale solar PV plants. *Prog. Photovolt. Res. Appl.* **2014**, *22*, 548–559. [CrossRef]
66. Zhu, W.; Wu, B.; Yan, N.; Ma, Z.; Wang, L.; Liu, W.; Xing, Q.; Xu, J. Estimating Sunshine Duration Using Hourly Total Cloud Amount Data from a Geostationary Meteorological Satellite. *Atmosphere* **2019**, *11*, 26. [CrossRef]